Synthesis and characterization of ceramic-polymer composite electrolytes for solid state batteries

Manuel Abellán Miñana

Directors: Marta Haro Remón, Alodia Orera Utrilla
UNIVERISITY OF ZARAGOZA

TABLE OF CONTENTS

ABSTRACT

Elemental lithium anodes are one of the most promising in batteries for electric vehicles because lithium has the lowest reduction potential, is the third lightest, and its cation is one of the smallest. A protocol for the synthesis and characterization of a composite polyethylene-oxide / $Li_{6.4}La_3Zr_{1.4}Ta_{0.6}O_{12}$ electrolyte containing LiTFSI as the lithium salt has been developed. The composite solid electrolyte (SE) has been compared with a reference polymer solid electrolyte. The composite SE has a Li^+ conductivity of $1.33 \cdot 10^{-5}$ S cm^{-1}, transport number of 0.59 and activation energy of 0.93 eV relate with those found in bibliography, which proves the protocol. Full solid-state Li-cells with a cathode based on $LiFePO_4$ have been tested. For that, the cathode composition, preparation, and assembling of the batteries have been stablished and optimized, and characterized with a liquid electrolyte, and later with the both the reference and composite SEs. The composite SE's cyclability is enhanced, and polarization reduced with respect to the reference. Capacities up to 100 mAh g^{-1} are reached.

RESUMEN

El uso de litio metal como ánodo en las baterías de los coches eléctricos es una de las opciones más prometedoras debido a que posee el potencial de reducción más negativo, es el tercer elemento más ligero y uno de los cationes más pequeños. Un protocolo para la síntesis y caracterización de un electrolito-sólido-compuesto basado en óxido de polietileno / $Li_{6.4}La_3Zr_{1.4}Ta_{0.6}O_{12}$ conteniendo LiTFSI como la sal de litio es desarrollado, posibilitando el uso de baterías recargables de Li metal en estado sólido. El electrolito-solido-compuesto (SE-compuesto) se ha comparado con un electrolito polimérico de referencia. SE-compuesto alcanza una conductividad para el Li^+ de of $1.33 \cdot 10^{-5}$ S cm^{-1}, un número de transporte de 0.59 y energía de activación de 0.93 eV, cuyos valores son equivalentes a los encontrados en bibliografía, probando así el protocolo. Se han hecho ensayos en baterías de litio de estado sólido con un cátodo basado en $LiFePO_4$. Para ello se han establecido rutas optimizadas tanto para la composición como para la preparación del cátodo, y para el ensamblaje de las baterías, y se han caracterizado con un electrolito líquido, y posteriormente con ambos SEs. La ciclabilidad del SE-compuesto mejora, y la polarización se reduce con respecto al de referencia. Se han alcanzado capacidades de hasta 100 mAh g^{-1}.

LIST OF ACRONYMS

μ_A	Anode electrochemical potential	LSV	Linear sweep voltammetry
μ_C	Cathode electrochemical potential	LUMO	Lowest unoccupied molecular orbital
AcN	Acetonitrile	NMP	N-methyl-2-pyrrolidone
CA	Chronoamperometry	PEO	Polyethylene oxide
CB	Carbon Black	PVDF	Polyvinylidene fluoride
DSC	Differential scanning calorimetry	SE	Solid electrolyte
E_A	Activation energy	SEI	Solid electrolyte interphase
E_F	Energy Fermi level	SEM	Scanning electron microscopy
E_g	Electrolyte's bandgap	SS	Stainless steel
EIS	Electrochemical impedance spectroscopy	t^+	Li^+ transport number
HOMO	Highest occupied molecular orbital	TGA	Thermogravimetric analysis
LCO	$LiCoO_2$	T_m	Melting temperature
LE	Liquid electrolyte	V_{OC}	Open circuit voltage
LFP	$LiFePO_4$ (oxidized/discharged state)	X_C	Crystallinity of the PEO matrix
LFP@CB	Commercial LFP-CB nanoshells	σ_{dc}	Ionic conductivity
LiTFSI	bis(trifluoromethylsulfonyl)amine lithium salt	σ_e	Electronic conductivity
LLZTO	$Li_{6.4}La_3Zr_{1.4}Ta_{0.6}O_{12}$		

1. INTRODUCTION

In the decade of the 90s a new rechargeable type of batteries appeared. With an unmatchable combination of high energy and power density, Li-ion commercialization was a success. Currently, as a potential hoarder of portable electronics, power tools and hybrid/full electric vehicles, research on Li batteries is as large as ever.

Batteries are electrochemical cells capable of exchanging chemical energy into electrical energy through reduction and oxidation processes. The main components are (i) anode, responsible of the oxidation reaction; (ii) cathode, which is where the reduction reaction occurs; (iii) electrolyte, a medium in contact with the two electrodes and whose function is to transport ions between them; and finally, (iv) collectors, which are simply metal connectors through which the released electrons, i.e., electric current, circulate. For a rechargeable battery, during the charge process the redox reactions in the electrodes exchange and electrical energy is converted into chemical energy.

Li-ion batteries are traditionally rechargeable batteries with transition metals containing lithium ion as the cathode and graphitic materials as the anode [1]. **Figure 1** shows a conventional Li-ion battery.
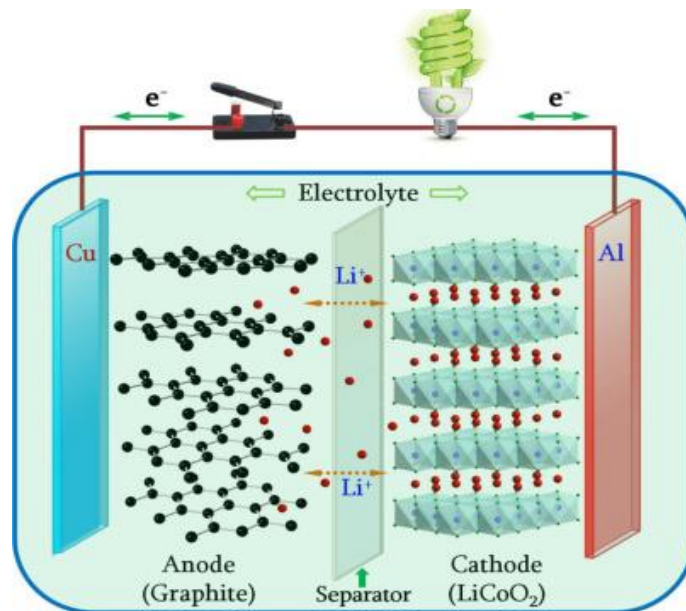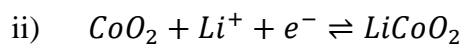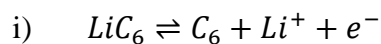

Figure 1. Illustration of a traditional Li-ion battery. Graphitic anode, lithium-transition metal-based cathode and liquid electrolyte are indicated.

In this case, the electrodes semi reactions for anode (i) and cathode (ii) are:

i) $LiC_6 \rightleftharpoons C_6 + Li^+ + e^-$

ii) $CoO_2 + Li^+ + e^- \rightleftharpoons LiCoO_2$

Shortage and rising prices of lithium are some of the most heard hassles in the popular opinion. Indeed, as available resources grow with the development of exploration and mining technologies, rising prices continue to do so. Cost related issues are the major factor inhibiting the expansion of Li-ion batteries into renewable energy applications. Even so, the lithium used in cathode and electrolytes is not the key factor in cost/prices. As a matter of fact, the cost of processing and the cost of cobalt in cathodes are the major contributing factors [2].

The market demands batteries with higher **rate capability**, which is the generation of considerable amounts of power with little polarization (voltage loss) even at high current loads, higher **charge capacity**, usually expressed in mAh, related to the energy stored in a battery, and (for cathodes) sufficiently **high voltage**, which, as will be explained below, is crucial to translate capacity into power. Energy and power densities of batteries improve by maximizing these properties, making them smaller and cheaper. A note must be made here. Materials and engineering are selected depending on their application, making them 'power optimized' or 'energy optimized'. Power is the product of intensity and the voltage provided by a cell, as equation 1:

$$P\,(W) = I(A) \cdot U(V) \tag{1}$$

As per usual, capacities and power are expressed in terms of the given property per one hour, thus a battery that supplies 3 Wh can support an uptake of 3 watts for 1 hour, or 6 watts during half an hour. And a battery with a capacity of 800 mAh and that provides 3.7 V; has 2.96 Wh of power, which is equal to 10656 J (1 J equals 1 Ws).

'Power optimized' batteries have high **rate capability** and are suitable for power-demanding electric vehicles; meanwhile, 'energy optimized' can supply more energy (high Wh) for mild loads (low currents) thus having greater **charge capacities** (high mAh) and suiting portable electronics better.

To conclude this preface, **cycle life** is the number of charge/discharge cycles until the capacity fades to 80% of its initial reversible value and it should provide over 30 000 safe cycles at an acceptable rate (equivalent to 10 years operational life) [3]. Besides, **cost** and **safety**, high **specific/volumetric energy density** (mAh/g or mAh/cm^3) and **shelf life** are additional figures of merit that may be achievable by optimizing and finding the most appropriate collector-electrode-electrolyte combination.

Electrodes and electrolyte

To advance in the most demanding energy requirements and sustainability it is necessary to advance in solid state Li batteries and remove the cobalt from the cathode. The first increases energy density and power as well as safety, and the second is required for sustainability, as discussed below.

Intercalation cathode materials

An intercalation cathode is a solid host network, which can store guest ions. The guest ions can be inserted into and be removed from the host network reversibly. In the case at hand, Li^+ is the guest ion and the possible network compounds are metal chalcogenides, transition metal oxides and polyanion compounds. They can be divided into several crystal structures, such as layered, spinel, olivine and tavorite. Metal chalcogenides, such as TiS_3, $NbSe_3$ or $LiTiS_2$, were studied long ago but exhibited partial reversibility due to irreversible structure change during lithiation (lithiation and delithiation are equivalent terms of discharging and charging). $LiTiS_2$ was eventually commercialized by Exxon. However, most current intercalation cathode research is focused on metal oxides and polyanion compounds due to its higher operating voltage, thus the higher energy storage. Typically, intercalation cathodes have 100-200 mAh/g specific capacity and 3-5 V average voltage vs. Li/Li^+.

$LiCoO_2$ (LCO) (cathode in **figure 1**) was introduced by Goodenough and is the first and most commercially successful form of layered transition metal oxide cathode. As so, John B. Goodenough, Stanley Whittingham and Akira Yoshino were rewarded the Chemistry Nobel prize in 2009 for their work in lithium-ion batteries. The Co and Li located in octahedral sites occupy alternating layers and form a hexagonal symmetry (**figure 2a**). The theoretical specific capacity can be calculated by Faraday's law of electrolysis by considering full conversion of active materials as:

$$Q_{theoretical}\left(\frac{Ah}{mol}\right) = \frac{nF}{3600\,M_w} \tag{2}$$

where n is the number of charge carrier (for Li^+ it is one), F is the Faraday constant (96485.3 As/mol), M_w is the host molecular weight in g/mol and the factor 3600 converts seconds into hours. LCO theoretical specific capacity of 274 mAh g^{-1} and volumetric capacity of 1363 mAh cm^{-3} are relatively high, low self-discharge, high

discharge voltage and good cycling performance are appealing properties, but the major limitations of cobalt's high cost, low thermal stability, and fast capacity fade at high current rates or during deep cycling (due to irreversible lattice distortion from hexagonal to monoclinic symmetry structure at ~50% delithiation) fostered strategies to palliate the limitations. Doping and partial substitution demonstrated promising and as a result, the $LiNi_{0.8}Co_{0.15}Al_{0.05}O_2$ cathode has finally found relatively widespread commercial use, for example, in Panasonic batteries for Tesla electric vehicles [2].

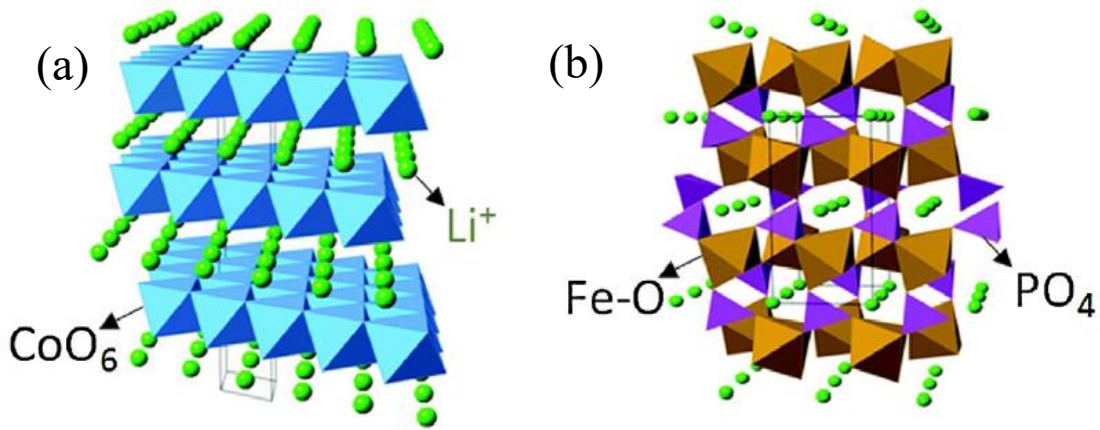*Figure 2. Crystal structures of representative intercalation cathodes: (a) layered $LiCoO_2$ and (b) olivine $LiFePO_4$. Layered and 1D organization of lithium cations in the crystal lattice can be easily observed in (a) and (b), respectively.*

Another family of intercalation cathode materials are polyanion compounds, where large $(XO_4)^{3-}$ (X = S, P, Si, Al, Mo, W) polyanions occupy lattice positions, which stabilizes its structure. $LiFePO_4$ (LFP) is the representative material, and the one studied herein. It has an olivine structure, and it is known for its thermal and electrochemical stability and relatively high power capability [2, 4]. Li^+ and Fe^{2+} occupy octahedral sites, while P atoms are in tetrahedral sites in a slightly distorted hexagonal close-packed oxygen array (**figure 2b**). Insertion of Li into the $FePO_4$ 1D channels gives a constant average potential of 3.45 V versus Li^+/Li^o in all the lithiation range. There is a small structural displacing of the framework between $FePO_4$ and $LiFePO_4$ as lithiation of the $FePO_4$ occurs (which is the discharge process). This two-phase character results in low electronic conductivity, which impedes electron movement to the collectors, and low ionic conductivity, which is an impediment for mass transference between electrode and electrolyte. Reduction of particle size in combination with conducting carbon coatings are found to be effective to increase electrical and ionic conductivity, thus rate performance improves. Its theoretical specific and volumetric capacities of 170 mAh g⁻

[1] and 589 mAh cm^{-3}, respectively, are sufficiently high. Low cost, natural abundance, environmental friendliness, thermal stability in the fully charged state and good cyclability are other attractive features of this material [5, 6].

Elemental lithium anode

Anode and cathode electrodes are electronic conductors with respective electrochemical potentials μ_A and μ_C, which may correspond to their Fermi energies ε_F in the case of metals, or to the energy of a redox couple of a transition-metal cation. The latter case being the Fe^{3+}/Fe^{2+} pair potential, and the former the lithium conduction-band. The energy difference E_g between the lowest unoccupied molecular orbital (LUMO) and the highest occupied molecular orbital (HOMO) of the electrolyte determines the electrochemical window, and the difference in the electrochemical potentials μ_A and μ_C is the open-circuit voltage V_{OC}.
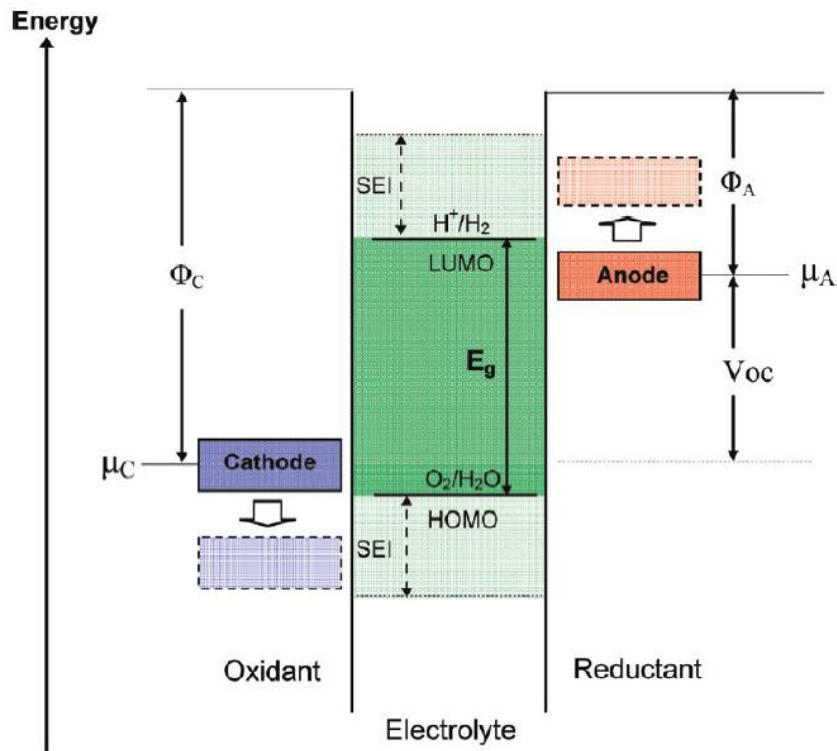

Figure 3. Schematic energy diagram of electrodes and an aqueous electrolyte.

Figure 3 schematizes the relative electron energies of the anode and cathode with an aqueous electrolyte with H^+ as mass carriers of the cell. To be thermodynamically stable, μ_A and μ_C must lie within the window of the electrolyte. Otherwise, the anode will reduce the electrolyte unless a passivation layer creates a kinetic barrier to electron transfer that blocks electron transfer from anode to LUMO, or the anode will oxidize the

5

electrolyte unless a passivation layer blocks electron transfer from cathode to HOMO. This barrier is the passivating solid/electrolyte-interface (SEI) layer [7, 8], and it must be permeable to the mass carrier and capable of rapidly adapting to the changing electrode surface area as the electrode changes volume during cycling. An SEI contributes to the impedance of the Li+ transfer across the electrode/electrolyte interface and lowers the cycle life of a battery cell.

The holy grail in next-generation batteries is accomplishing a safe and practical lithium metal-anode battery. Lithium provides the highest theoretical capacity (3,860 mAh g^{-1} or 2,061 mAh cm^{-3}) and lowest electrochemical potential (-3.04 V versus the standard hydrogen electrode). To put together this data: LiC$_6$, an extensively displayed anode material, has an electrochemical potential of 0.5-1.2 V vs. Li/Li$^+$, and, as it accommodates one lithium ion per hexagonal cell of sp^2 carbons, a smaller capacity of 340 mAh g^{-1}; lithium-ion batteries reach a specific energy of ~250 Wh kg^{-1}, an order of magnitude lower than practical value of petrol, on the other hand, a Li anode/lithium-transition metal oxide cathode (as LFP) can deliver a specific energy of ~440 Wh kg^{-1} [8].

The reasons of its oblivion for several decades are several safety concerns, high chemical reactivity, virtually infinite relative volume change (hostless matrix), and dendrite growth (**fig 4**). Lithium's Fermi level lies above the LUMO of known practical nonaqueous liquid electrolytes. Luckily, SEI layer formation allows its use as anode in half-cells, but on repeated charge/discharge cycles, cracking of the SEI layer in selected areas (due to volume changes in the electrodes) results in the formation of dendrites that grow across the electrolyte, short-circuiting the cell and ultimately causing a thermal run-away reaction that might cause the battery to catch on fire, potentially ending in an explosion.

Figure 4. Optical microscope image of a Li dendrite [30].

6

Thanks to development of research tools and nanotechnology-based solutions, elemental lithium anodes are ready for revival. One of them being the solid electrolyte.

It must be noted that secondary anode materials are also a great topic of research but their study is beyond the scope of this work [9].

Composite solid electrolyte

As explained above, similarly to many other metals, Li tends to deposit in dendritic form. In the context of a cell, on charging, Li^+ travels through the electrolyte from the cathode to the anode, where it reduces to Li^o. Inhomogeneities in the anode surface where density of electrons is greater, preferential pathways for the diffusion of the lithium cation in the electrolyte, instability of a SEI layer, disordered spatial Li-ion distribution in the electrode's surfaces, etc. creates 'hot spots' where the reduction reaction is promoted. The protrusions are conductive points that bring the electrodes closer to one another and have considerably higher electric fields at their tips. Furthermore, they enable faster three-dimensional Li-ion diffusion, rather than 1D diffusion observed in flat surfaces. Therefore, it is not a surprise that those little deposits of lithium grow rapidly owing to its self-enhanced growth nature [8, 10] .

One way to address the challenge of dendrite growth of lithium metal at the anode is the use of all-solid-state rechargeable batteries. **Table 1** summarizes some of the properties that must be possessed by a solid electrolyte (SE) for lithium batteries, and its effect on battery performance.

Solid electrolytes are usually classified in polymer-based membranes and inorganic/ceramic-based materials. Ceramic SEs are based on oxides, sulphides, nitrides, hydrides, halogenides, borates and phosphates, while organic are based on polymers [11]. Each family provides advantages and inconveniences. As expected, up to date there is no material meeting all the requirements and new concepts are currently being designed including the preparation of polymer-ceramic composites. Composites are, per definition, physical mixtures of two constituents with no interfacial bonding. This blending approach can help achieving target performances via addition of properties as well as offering synergic or even enhanced functionalities: improved electrochemical stability, ionic conductivity, and mechanical properties.

	Material's property	Effect on solid-state battery performance
1	Large/sufficient electrolyte window, Eg; >4.5V for Li anode	Higher cell voltage and energy density; long-term stability, lifetime
2	Retention of electrode/electrolyte interface; intimate interface contact with electrodes	Low charge-transfer resistance; high current, high power, long-term stability
3	Li$^+$ ion conductivity σ_{Li}>0.1 mS/ cm^{-1} over temperature range of battery operation	High current density and high power
4	Dielectric behaviour (electronic conductivity σ_e<10^{-10} S cm^{-1}), and transference number close to 1	Minimizes self-discharge rate, maximizes usable voltage (energy density), and favours dissociation of ionic aggregates
5	Chemical stability over T operation range, and inertness against electrode materials	Long-term stability, lifetime
6	Enough elastic modulus; mechanically flexible and robust, allowing self-standing or electrode-supported membranes of thickness 10-30 µm	Avoid Li dendride growth, maximizing safety; facilitates lamination process and avoids fractures during cell assembly and lithiation/delithiation cycles
7	Non-flammable and nonexplosive materials if short-circuited	Assesses safety issues
8	Low toxicity and low cost (abundant)	Reduces manufacturing costs and minimizes safety issues
9	Solution-based processing	Industrially scalable

Table 1. Requirements of a solid electrolyte for application in all-solid-state batteries [5, 8, 12, 13].

Polymeric electrolytes such as PEO membranes are blends of a polymer matrix and a salt. In general, they benefit from good stability against elemental Li, flexibility, scalability, and low shear modulus, but thermal stability and insufficient ionic conductivity are important drawbacks [14, 15]. The matrix should have a high dielectric constant and electron-donor characteristics provided by polar groups such as ether (—O—) to facilitate dissociation of the salt. The charge transfer is provided by segmental motion assisted diffusion mechanism, as reproduced in **figure 5**. It ocurrs in the amorphous region of the network by association/dissociation of the ion with the polar groups, being inter- or intra-chain.
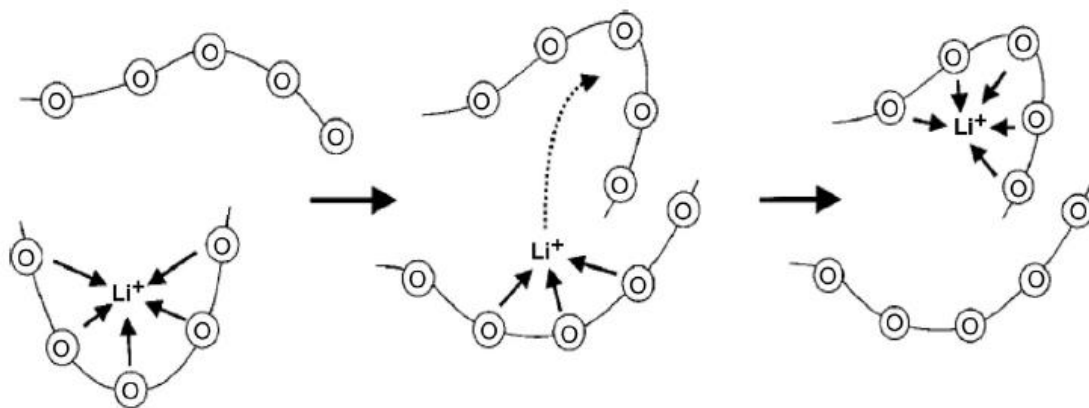
Figure 5. Schematic of segmental motion assisted diffusion mechanism of Li$^+$ in a PEO matrix.

The charge transfer is possible for both positive and negative ions of the salt. The most used salt with PEO is bis(trifluoromethylsulfonyl)amine lithium salt (LiTFSI). LiTFSI is a PEO soluble salt whose anion delocalizes negative charges and favours dissociation, freeing Li$^+$ and boosting ionic mobility. TFSI$^-$ anion is big and polarizable, hence its mobility in the network is low, which gets reflected in higher transport numbers for the lithium cation. Furthermore, addition of impeded lithium salts decrease crystallinity of the PEO matrix, increasing amorphous phase and ionic conductivity [14, 16].

Inorganic ceramic electrolytes exhibit satisfactory ionic conductivity, some of them even surpassing that of liquid electrolytes; although it is very sensible to changes in the crystalline lattice. They conduct through defective or interstitial sites at the local atomic scale. Chemical, electrochemical, and mechanical stability profits are traded off by low surface adhesion, resulting in deficient interfacial contacts between the SE and the electrodes [17].

LLZTO is one of the most promising ceramic nanofiller. Its garnet-type structure can be prepared in the cubic or tetragonal form depending on the ceramic synthesis route. Arrangement of the tetrahedral units in the cubic form leads to the existence of interconnecting octahedral sites which can be occupied by Li$^+$. Increasing the number of lithium atoms in the molecular formula from 5 to 6.4; and doping with Ta, increases ionic conductivities from ~10^{-6} to ~10^{-4} S cm^{-1} at 25 ℃ for $Li_5La_3M_2O_{12}$ and $Li_{6.4}La_3Zr_{1.4}Ta_{0.6}O_{12}$, respectively. The tetragonal form shows two orders of magnitude lower room temperature ionic conductivity than the cubic. To stabilize the latter, small concentrations of Al in the order of 1 wt% were sufficient, which can be achieved by preparing the ceramic material in Al_2O_3 crucibles [13, 18].

Figure 6 shows the chemical structures of the components in the SE prepared in this work.
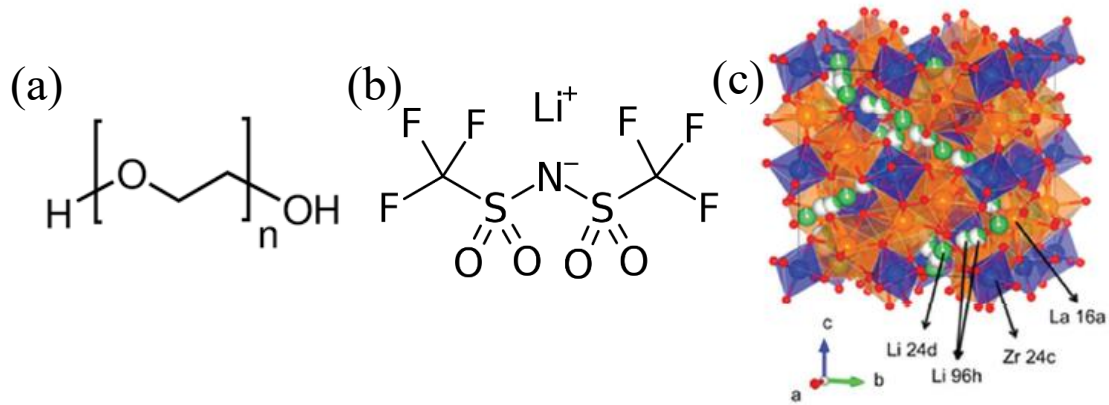

Figure 6. Chemical structures of the main components of the composite electrolyte membranes: (a) PEO, (b) LiTFSI and (c) LLZTO [18].

In a composite solid electrolyte, when addition of the ceramic component surpasses a critical %vol (percolation threshold) the mechanism of ionic conduction shifts with the apparition of alternative Li^+ transfer pathways [19]. The conductivities will be mainly determined by the polymer chain movement when the LLZTO content is less than the percolation threshold. With percolation (example in **figure 7**), the conductivities are provided by both the transfer pathways of the polymer and LLZTO [16, 20].

The procedure in this work is to disperse ceramic particles of $Li_{6.4}La_3Zr_{1.4}Ta_{0.6}O_{12}$ (LLZTO) as the ceramic nanofiller in a polyethylene oxide (PEO) matrix with bis(trifluoromethylsulfonyl)amine lithium salt (LiTFSI). The final solid-state-battery with a lithium anode, a composite solid electrolyte and a cathode based on LFP is schematized in **figure 7**.
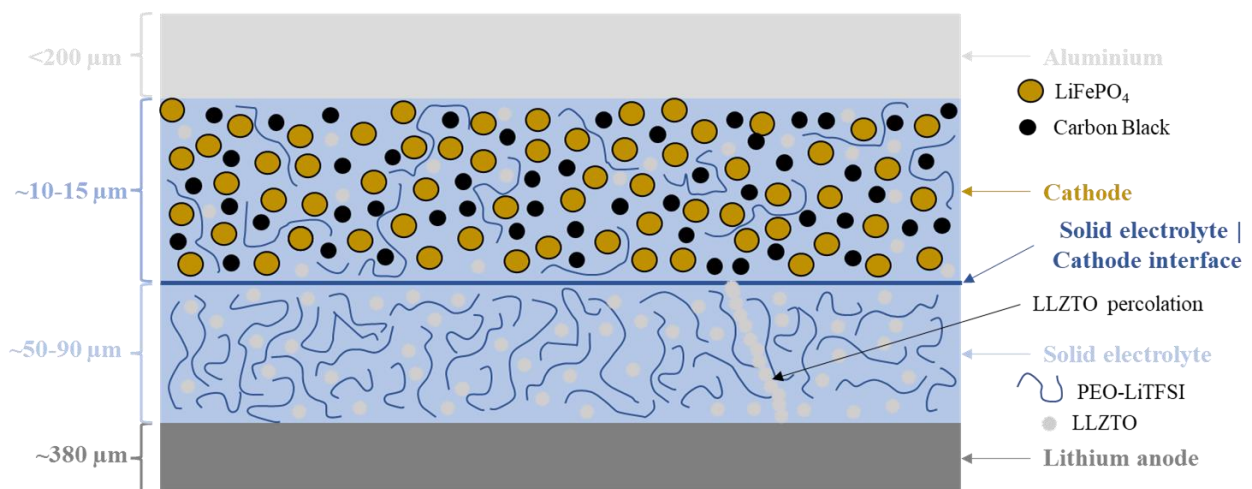

Figure 7. Schematic figure of the final solid-state-batteries prepared herein: lithium as anode, composite solid electrolyte, and cathode based on LFP with catholyte as binder. LLZTO percolation is indicated for educational purposes. Not in scale.

2. OBJECTIVES

This Final Master Project is an autonomous work under the supervision of two tutors, within two research groups, showing the project's interdisciplinarity. The work is divided in the following objectives:

- Preparing and optimizing a composite solid electrolyte based on the PEO-LiTFSI complex with enhanced stability due to addition of ceramic material LLZTO.

- Developing and optimizing a preparation protocol for cathode based on two different commercial $LiFePO_4$ materials. The system is to be characterized with a liquid electrolyte. To improve cathode-SE interphase contact, a binder with the same composition as the SE (catholyte) is added and checked with a liquid electrolyte.

- Incorporation, conditioning, and characterization of the full cells with lithium metal.

The experimental work has been carried out in the Physical Chemistry Department in the Science Faculty and the Ciencia y Tecnología de Materiales y Fluidos, EINA.

3. EXPERIMENTAL

3.1. Sample preparation and assembly

Solid electrolyte membrane preparation

Reference and composite membranes were prepared by casting method. Reference polymer-based SE membranes consisted in a mixing of polyethylene oxide (PEO powder, Sigma Aldrich, average M_v 600,000) and lithium bis(trifluoromethane)sulfonimide salt (LiTFSI, 99.9%, Sigma Aldrich), with a fixed molar composition of 18:1 (EO : Li), in acetonitrile (AcN, anhydrous synthesis grade, Fisher Scientific). This composition corresponds to a membrane with 73 wt% of PEO and 27 wt% of LiTFSI. Polymer-ceramic composite membranes were prepared by maintaining the 18:1 (EO:Li) molar ratio and adding a 30 wt% of $Li_{6.4}La_3Zr_{1.4}Ta_{0.6}O_{12}$ (LLZTO, >99.9%, D50 400-600 nm, Ampcera^{TM}) resulting in a composite membrane composition with 51 wt% of PEO, 19 wt% of LiTFSI and 30 wt% of LLZTO. After 24h of mixing, the viscous liquid was casted into a teflon petri dish of ~7 cm diameter and dried in dynamic vacuum. To avoid compromising the membrane morphology by boiling of the solution, pressures were gradually increased from low to higher vacuums. After 24h of drying, the plastic-like membranes were carefully separated from the teflon dish and placed in between *Mylar* sheets, which act as humidity barriers and facilitate manipulation. Easy thickness control is achieved by varying the amount of solution into the petri dish. In this work, a fixed mass of ~3.7 g was weighted for each membrane. **Table 2** shows label, weight of components and solvent volume necessary in the preparation of the three characterized membranes.

Label	PEO (g)	LiTFSI (g)	LLZTO (g)	AcN (mL)
REF	0.5	0.1811	-	10
LLZ-10	0.35	0.1268	0.2043	10
LLZ-7				7

Table 2. Composition of the three studied solid electrolyte membranes

LiTFSI, LLZTO and the prepared membranes were stored in an Ar globe box due to its hygroscopic properties.

Cathode preparation

Cathode preparation consisted in LiFePO$_4$, Super P Carbon Black (CB, AlfaAesar) and one of two binders, polyvinylidene fluoride (PVDF, AlfaAesar) or 'catholyte', which is the electrolyte solution above. The components were solved in a small amount of N-methyl-2-pyrrolidone (NMP, Extra Dry, for Synthesis, Fisher Chemical™). The solution was hand-mixed in an Agatha mortar until a slurry formed, then it was casted into an aluminium foil. A Film Casting Doctor Blade was used to control cathode thickness by modifying its height during casting of the slurry. The height was fixed to 20 or 30 µm. The casted slurry is immediately dried in a heating plate and further dried for 12 hours at 120 ℃ in vacuum. The wt% of each component and the binders varied throughout the research, so did the rheology of each slurry, hence the mixing methodology had to be adapted. For PVDF binder, the powders were mixed in a mortar and NMP was added dropwise until slurry texture was suitable for the casting-drying processes. For the catholyte binder, all components, including a fixed volume of NMP, were mixed for 24 hours before casting.

LiFePO$_4$ (LFP, >97%, <5 µm particle size (BET), Sigma-Aldrich) and LFP-CarbonBlack nanoshells (LFP@CB, D50 13.74 µm, Advanced Lithium) were studied in this work as the active component of the cathode. They were stored in the Ar globe box.

Device manufacturing

Many of the characterization and measurements in this work make use of lithium foil (0.38 mm thickness, Sigma-Aldrich) in the device. Lithium reacts with the atmosphere and N$_2$, which is why all batteries were set up in an Ar glovebox in button cells type CR2032. The manufacturing consists in assembling the electrodes and electrolyte disks between two stainless steel (SS) collectors and inside the button cell. A SS spring is also incorporated inside the cell. The devices are sealed with a press force ca. 70 kg·cm^{-2} (manual hydraulic press, TMAXCN). Cathode, SE, and lithium disks were cut with diameters of 8, 15 and 9 mm, respectively. $\emptyset_{cathode}<\emptyset_{lithium}$ ensures cycling of all the cathode loading, while $\emptyset_{eletrodes}<\emptyset_{electrolyte}$ avoids electrode contact/short-circuiting. Cathodes were first characterized in half-cells against Li^o with a liquid electrolyte (LE). LE assembly consisted in the addition of 100 µL of LiPF$_6$ solution 1.0 M in ethylene carbonate : diethylene carbonate 50/50 (v/v) (Sigma-Aldrich) in a glass microfiber filter (Whtamann GF/C^{TM}).

3.2. Material characterization

Thermal characterization: thermogravimetric analysis and differential scanning calorimetry

The thermal behaviour of the SE was investigated by thermogravimetric analysis (TGA) and differential scanning calorimetry (DSC). TGA was performed in 2960 SDT instrument from ambient temperature to 170 ℃ in a nitrogen atmosphere in alumina pans. DSC analysis was performed in DSC Q20 V24.10 Build 122 instrument in a nitrogen flow of 50 mL/min and a Tzero Aluminum Hermetic pan. Three ramps were performed at 1 ℃/min: heating from 25 ℃ to 100 ℃, cooling to 25 ℃ and heating again to 100 ℃. Crystallinity of the PEO matrix (X_C) was calculated by DSC by equation 3:

$$X_C = \frac{\Delta H_m}{\Delta H_{PEO} f_{PEO}} \cdot 100\% \tag{3}$$

where ΔH_m is the melting enthalpy of the electrolyte and corresponds to the area of the melting transition peak in heat flow vs time heating curves, ΔH_{PEO} is the value of ΔH_m for PEO in its fully crystallized form (203 J g^{-1}), and f_{PEO} is the PEO mass percentage in the electrolyte. The crystalline melting temperature (T_m) corresponds to the local maximum of the heating curves [12].

Microstructure and thickness evaluation: scanning electron microscopy and confocal microscopy

Thickness and rugosity of the SE was analysed by confocal microscopy using a Confocal SENSOFAR PLµ 2300 apparatus.

Further microstructure analysis of SE and the cathode laminates was carried out by scanning electron microscopy (SEM) using Zeiss FESEM MERLIN instrument operated at a voltage of 5 or 10 kV, using the secondary electron detector. The SE cross section samples were prepared by breaking the frozen membranes inside liquid nitrogen (below the glass transition temperature of the PEO matrix, -58 ℃) [21]. Samples of the cathode laminates were gently teared apart to expose the cross section. SE and cathode laminates were coated by Au and C, respectively.

3.3. Electrochemical characterization

Cycling performance

Cycling performance of the cathodes in the assembled semibatteries (using liquid or synthesized solid electrolyte) was tested and different conditioning procedures evaluated. Each test consists of 3 cycles at different rate of discharge/charge: 0.1C, 0.2C, 0.5C, 1C and 5C, using a Autolab M204 potentiostat or a homemade cycling apparatus at ambient conditions. The lower and upper cut-off voltages were fixed to 2 and 4 V, respectively. To prevent irreversible degradation and failure of the cell in case that the cut-off voltages could not be reached, each cycle was limited in time with a time value slightly larger than the selected C rate (for example 15 hours at 0.1C).

Electrochemical window, ionic conductivity, activation energy and transport number calculations of the solid electrolytes

The LUMO energy values were approximated to be the oxidation voltage of the SE. Therefore, lineal sweep voltammetry (LSV) in asymmetric Li|SE|SS cells was performed to obtain the electrochemical window of the electrolyte. Potentials from 2.5 to 6.0 V at 1 mV s^{-1} were tested [11, 20, 22].

Ionic conductivity and activation energy calculations were performed in ion-blocked symmetric cells consisting in SE supported between SS current collectors. Electrochemical impedance spectroscopy (EIS) in the frequency range of 1 MHz to 1 Hz was carried out. According to the salt in polymer model [23] it is possible to directly estimate 'real conductivity' (σ') as a function of the frequency from the impedance data as:

$$\sigma' = \frac{l}{A} \frac{Z'(\omega)}{(Z'(\omega))^2 + (Z''(\omega))^2} \qquad (4)$$

where l is the thickness and A the area of the SE, $Z'(\omega)$ and $Z''(\omega)$ are the real and imaginary impedances, respectively.

In log σ' versus frequency (ν) representations, log σ' values grow until they reach a plateau. The σ' is recorded at a range of temperatures, and the values independent from frequency are the ionic conductivity (σ_{dc}). Activation energy and σ_{dc} at 30 ºC are obtained by fitting the data to Arrhenius plots according to equation 5:

$$\sigma_{dc} = \sigma_0 \exp\left(-\frac{E_A}{k_B T}\right) \qquad (5)$$

where σ_0 is a preexponential factor, E_A is the activation energy, k_B is Boltzmann constant and T each temperature of measurement.

The transport number of Li$^+$ (t$_+$) was calculated according to the Evans and Bruce method [24]. The SE is supported between two lithium metal disks so charge transference is not blocked. Combination of EIS-chronoamperometry (EIS-CA) measurements are used to calculate t$_+$, following:

$$t_+ = \frac{I_{ss}(\Delta V - I_0 R_0)}{I_0(\Delta V - I_{ss} R_{ss})} \qquad (6)$$

where I_0 and I_{SS} are the currents (in A) across the SE initially, and in a stationary state consequence of a polarization due to an applied voltage of 10 mV; and R_0 and R_{SS} are the resistance values obtained from the EIS measurements before and after polarization, respectively.

Autolab M204 equipment was used for the three measurements. A homemade temperature controller was used for the conductivity and energy activation measurements. Considering Li disk's thickness to be almost equal to that of the SS disks, 'inside pressure' is maintained in all cells by adding an SS disk when necessary. This results in 3 SS and 1 Li disk for LSV cells, 4 SS for σ_{dc}/E_a, and 2 SS and 2 Li for t$^+$ calculations.

4. RESULTS AND DISCUSSION

4.1. Solid electrolyte

REF, LLZ-10 and LLZ-7 solid electrolytes were prepared and characterized by SEM. Surface and profile can be observed in **figure 8**. Average thicknesses for REF, LLZ-10 and LLZ-7 are 85, 52 and 68 µm respectively, and agree with those measured by confocal microscopy (**figure S3, S6 and S8**), which is a simpler and less time-consuming microscopy. Spherulites binded by polymeric excess is the characteristic microstructure of PEO-LiTFSI system [12]. Some spherulites can reach diameters similar to the electrolyte's thickness (observable in REFs profile), thus creating preferential channels for Li deposition and dendrite growth [8]. Addition of ceramic

particles is accompanied by loss of that texture, becoming a much more compact one. The wave-like pattern observable in LLZ-10 and LLZ-7 only appears in one of the faces of the SE. It corresponds to the machining in the teflon petri dishes where the electrolytes are deposited and dried, as confocal microscopy images confirmed. SEM images reveal significant differences in the LLZ-10 and LLZ-7 samples. The latter sample shows a cracked surface indicating the formation of a more brittle electrolyte, that may be related to less homogeneous mixing/drying phenomena. Also, cycling of the corresponding cell gave unimpressive performance which is explained below ('Incorporation of LLZTO into the cathode – solid electrolyte system'). Contrariwise, preparation of a composite SE with 10 mL of AcN resulted in the LLZ-10 membrane, which is homogeneous, smooth, uncracked, and where LLZTO particles are well dispersed. Therefore, the succeeding characterization will only be of REF and LLZ-10.
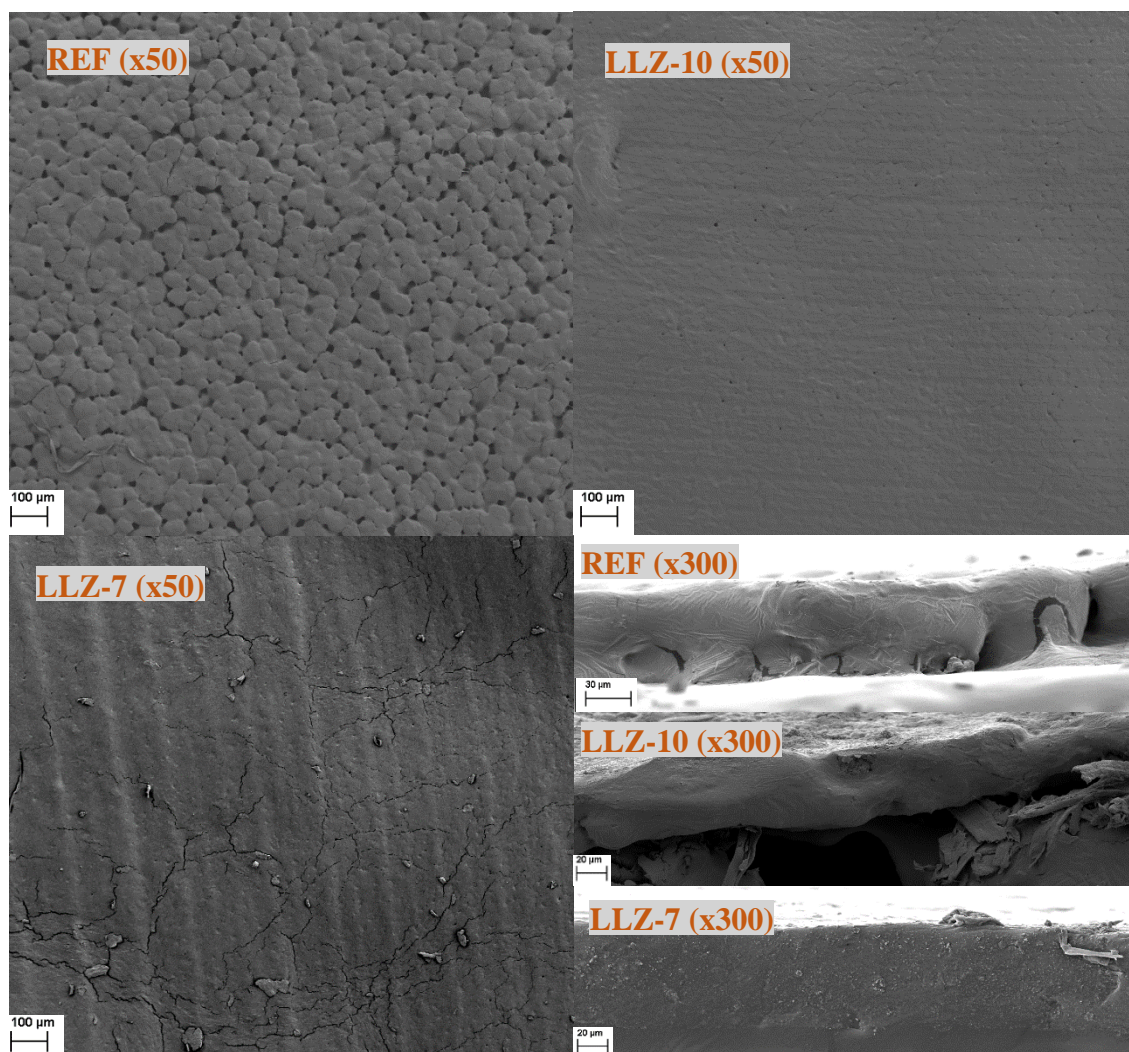
Figure 8. Surface and profile SEM images of REF, LLZ-10 and LLZ-7 at 5 and 10 kV. Loss of spherulitic texture with the addition of LLZTO is very notable.

Crystallinity and T_m were studied by DSC analysis and the results are summarized in **table 3**. Heating – cooling – heating ramps from 25 to 100 ºC were carried out for REF and LLZ-10 (**figure S9-S16**) before and after a thermal treatment of 70 ºC for 15 hours (samples will be referred as Pre-REF, Post-REF, Pre-LLZ-10 and Post-LLZ-10). This thermal treatment, 'T-treatment', is the fully optimized conditioning performed on batteries before cycling and will be introduced in section ('LFP@CB and solid electrolyte conditioning'). The data show melting temperatures are insensible to LLZTO's addition, probably because there is not an interfacial bonding between the ceramic material and the polymeric matrix. On the contrary, crystallinity increases slightly with addition of LLZTO particles, which may act as "anchors" where the polymer chains can stabilize and form crystalline structures. Both melting temperature and crystallinity drop from the first heating to the second one in each sample. This reveals that fast/forced cooling decreases crystallinity by rapid accommodation of the polymeric chain. On the contrary, comparison of samples with and without T-treatment disclose a small increase (practically within the experimental error of the calculation) in crystallinity ascribed to slow cooling (at ambient conditions) and lower T reached (70 ºC vs. 100 ºC), which allows accommodation of the polymeric chains in a more stable/organized structure. One could establish a parallelism between this behaviour and thermodynamic versus kinetic reaction control, where a product A is formed faster than B even though the latter is thermodynamically more stable.

Sample	Heating cycle	T_m (ºC)	ΔH_f (J/g)	X_C (%)
Pre-REF	1st	47.8	36.31	24.4
	2nd	46.0	28.47	19.1
Post-REF	1st	48.3	38.06	25.5
	2nd	45.0	27.09	18.2
Pre-LLZ-10	1st	47.1	33.51	32.1
	2nd	45.3	20.69	19.8
Pre-LLZ-10	1st	48.0	30.73	29.5
	2nd	45.3	15.86	15.2

Table 3. Melting temperature, melting enthalpy and crystallinity calculated by DSC analysis.

TGA was carried out from ambient temperature to 175 ºC. REF and LLZ-10 show constant weight loss up to 3.5% and 1.3%, respectively (**figure S17**). This behaviour may indicate little hydration. The difference of 2.2% may be due to LLZTO's less hygroscopic nature than LiTFSI. Small peaks between 74 and 86 ºC correspond to acetonitrile's boiling point (82 ºC) and it may indicate that the drying process could be optimized a bit further.

To estimate the ionic conductivity (σ_{dc}) and E_a of REF and LLZ-10 electrolytes, **Figure 9a** shows the dependence of the logarithm of the ionic conductivity (determined using equation 5) against the inverse of the temperature (σ' vs. frequency in **figure S18-19**). This dependence is lineal at $T < T_m$, indicating Arrhenius behaviour, range within is possible to calculate E_a according to equation 5. When $T > T_m$ there is deviation from the Arrhenius behaviour, which is related to greater coupling of the ionic diffusion (mechanism typical of liquids) and the polymer segmental relaxation (SE typical mechanism). LSV curves in **figure 9b** show that the electrochemical window is up to 4.5 V, which is more than adequate for commercial batteries.

Table 4 collects the values calculated for ionic conductivity, activation energy and Li+
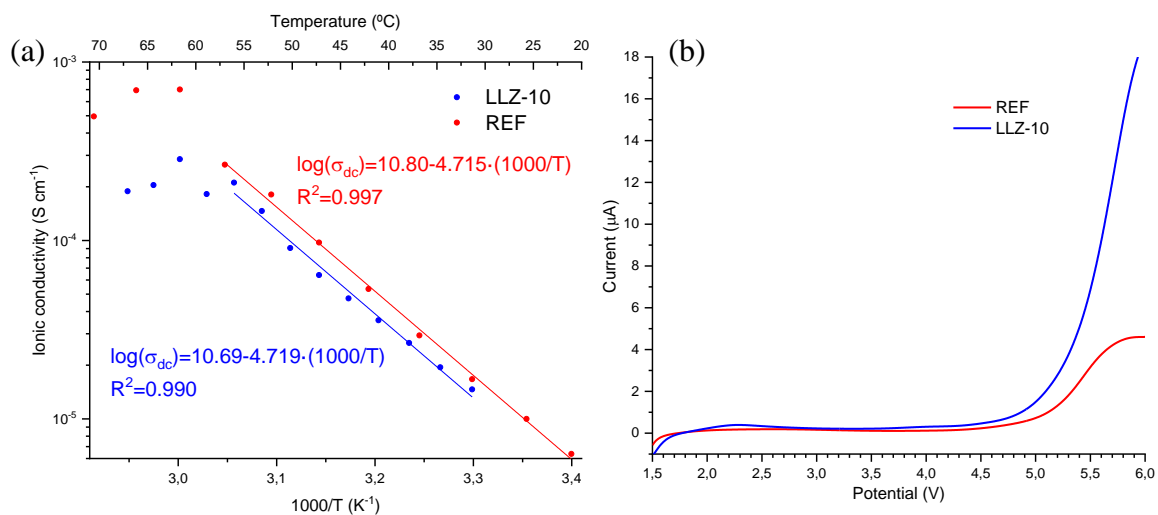
Figure 9. (a) Arrhenius plot of the ionic conductivity vs. 1/T and (b) LSV curves showing the oxidation potentials of the two SE.

transport number (EIS and CA curves in **figure S20-21**) for both membranes. Lithium transport numbers were estimated by an adapted methodology based on Evans and Bruce's one. The obtained values (0.54 and 0.59 for REF and LLZ-10) are above typical values recorded in bibliography, which are around 0.25 to 0.5 values [20, 25, 26]. The obtained ionic conductivity and activation energy values agree with those found in the

literature [20, 27] . When adding 30 wt% LLZTO material, σ_{dc} decreases ~25%, and activation energy remains unaltered. These two observations agree with the theory the ionic conduction in the synthetized electrolytes corresponds to the segmental motion mechanism typical of the PEO-LiTFSI system. Conduction through defective or interstitial sites at the local atomic scale, which is characteristic of ceramic materials, would appear when a critical vol% of LLZTO was surpassed, activating a percolation effect [16]. Other conduction mechanism can activate in hybrid solid electrolytes by bonding the ceramic material with the polymeric matrix [13].

Solid Electrolyte	T_m (ºC)	X_C (%)	σ_{dc} / 30ºC (S cm^{-1})	E_A (eV)	t_+
REF	47.8	24.4	$1.76 \cdot 10^{-5}$	0.93	0.54
LLZ-10	48.1	25.5	$1.33 \cdot 10^{-5}$	0.93	0.59

Table 4. Melting point, crystallinity and electrochemical characterization values obtained for the two studied electrolytes.

None of those new conduction mechanism is activated in the membranes prepared herein, but great improvements in cycling stability will be remarked in the following sections.

4.2. Cathode

LFP selection – study with a liquid electrolyte

LFP, LFP/C and LFP@CB cathodes were studied by cycling of half-cells against Li metal. They were assembled with liquid electrolyte (LiPF$_6$). **Table 5** shows the treatment, composition and the resulting specific capacities calculated at 0.1C rate for the seven characterized batteries.

Label	LiFePO$_4$	Ball milling	CB (%)	Binder (%)	Specific discharge capacities (mAh g^{-1})
M1	LFP	No	20	10 PVDF	11
M2	LFP	LFP	20	10 PVDF	11
M3	LFP/CB	LFP + 10 wt% CB	20	10 PVDF	138
M4	LFP/CB	LFP + 10 wt% CB	0	10 PVDF	13

M5	LFP@CB	No	0	5 PVDF	163 – 16
M6	LFP@CB	No	20	5 PVDF	166
M7	LFP@CB	No	20	5 catholyte	165

Table 5. Specific capacity resulting from the cycling of the 7 characterized batteries with 3 different LFP material: (i) LFP is the raw material from Sigma-Aldrich; (ii) LFP/CB when the first is ball milled with Carbon Black and (iii) LFP@CB is a commercial core-shell LFP with CB, provided by Advanced Lithium.

Capacities of LFP powder with no pre-treatment (ca. 11 mAh g^{-1}) were strikingly below the theoretical capacity of 170 mAh g^{-1}. Many studies emphasize the importance of microstructures in porous electrodes in their capability, so a deagglomeration/size reduction step by ball milling (3 cycles of 20 minutes) before hand-mixing in the mortar was tested. Ball milling of LFP plus a 10 wt% of CB (M3) showed great improvement, while the same treatment of LFP alone (M2) did not. Therefore, this capacity enhancement is a result of reduction size and deagglomeration of CB, and well dispersion of the conductive additive during the ball milling treatment (**figure 10** – structures 1 and 2). During the slurry preparation a CB film covers the LFP particles, which gets settled at the drying step (**figure 10** – structure 3). This combination of steps provides of homogeneous pathways or networks that go around the active material particles.
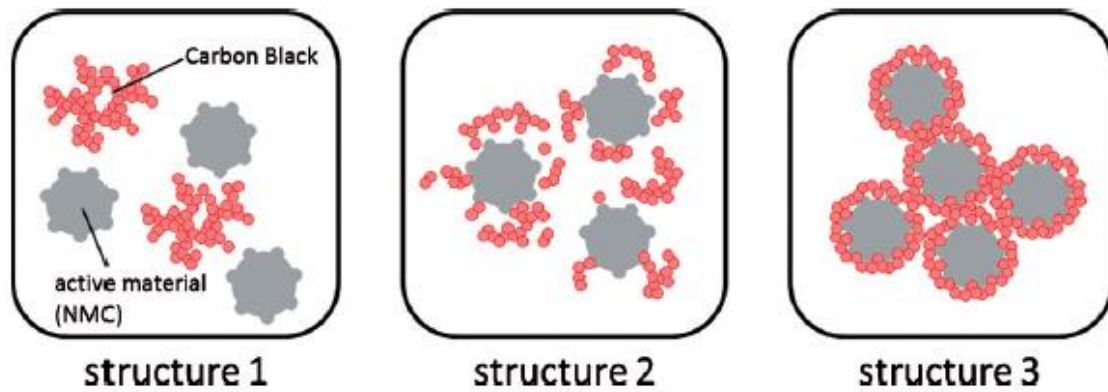
Figure 10. Particle structures along the LFP/CB cathode preparation [31].
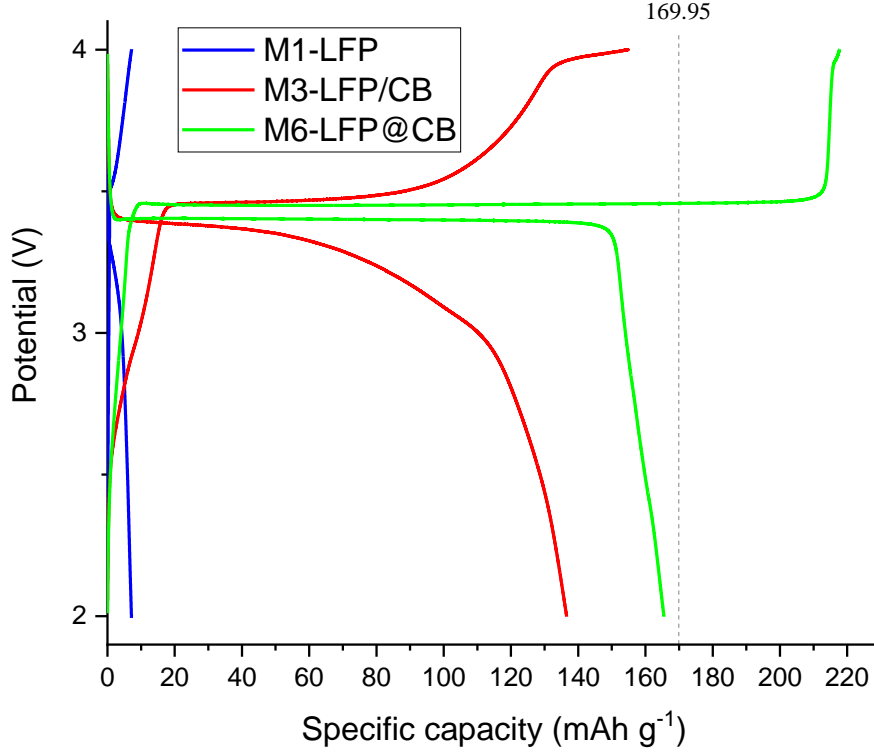
Figure 11. Voltage profiles of the third cycle at 0.1C of cathodes 1, 3 and 6. Very different capacity values are related to microstructure of the distinct cathode material and preparation procedures.

The voltage profiles of the third cycle at 0.1C of samples 1-LFP, 3-LFP/CB and 6-LFP@CB (**figure 11**) show the improvement along the experiments, almost reaching theoretical values for the LFP@CB cathode. Commercial LFP@CB consist in LFP particles covered in a nanoshell of CB, therefore microstructure is provided, and ball milling is not performed to preserve the structure intact. The large plateau region for LFP@CB material is related to several factors [28]: (i) low drop in cell voltage due to current flowing across the battery's internal resistance, (ii) low activation polarization, or the inherent kinetic factors of an electrochemical reaction, and (iii) low concentration polarization, which is the factor that considers the resistance faced by the mass transfer process by which ions are transported across the electrolyte from the lithium metal to the cathode. When close to the fully charged/discharged states, the concentration polarization dominates due to Li^+ ions building up in the electrodes, and the slope of the curve becomes very steep. Low hysteresis in the plateau regions of charge/discharge indicates a very reversible electrochemical reaction, meaning lithiation/delithiation processes occur at close voltage values.

The percent Coulombic efficiency of a single cycle associated with a capacity fade is calculated as $\frac{Q_{discharge}}{Q_{charge}} \cdot 100$. The Coulombic efficiency of LFP and LFP/CB cells is up

22

to 90%, but LFP@CB shows a somewhat abnormal charge capacity, resulting in a value of ~80%. This behaviour will be discussed below. Coulombic efficiency and discharge capacities vs. Cycles of all the referred batteries in this work are represented in **figure S22** to **figure S35**.

As the catholyte and the solid electrolyte have the same composition, including it as a binder in the cathode structure should upgrade, even fuse, interfacial contact between the electrode and the SE. As explained in 'Cathode preparation', the preparation had to be adapted. To assure that microstructure and properties of the cathode maintains from one binder to another, this cathode was also tested with a liquid electrolyte in sample 7. **Figure 12** compares the voltage profiles of PVDF vs. catholyte binders in samples 6 and 7.
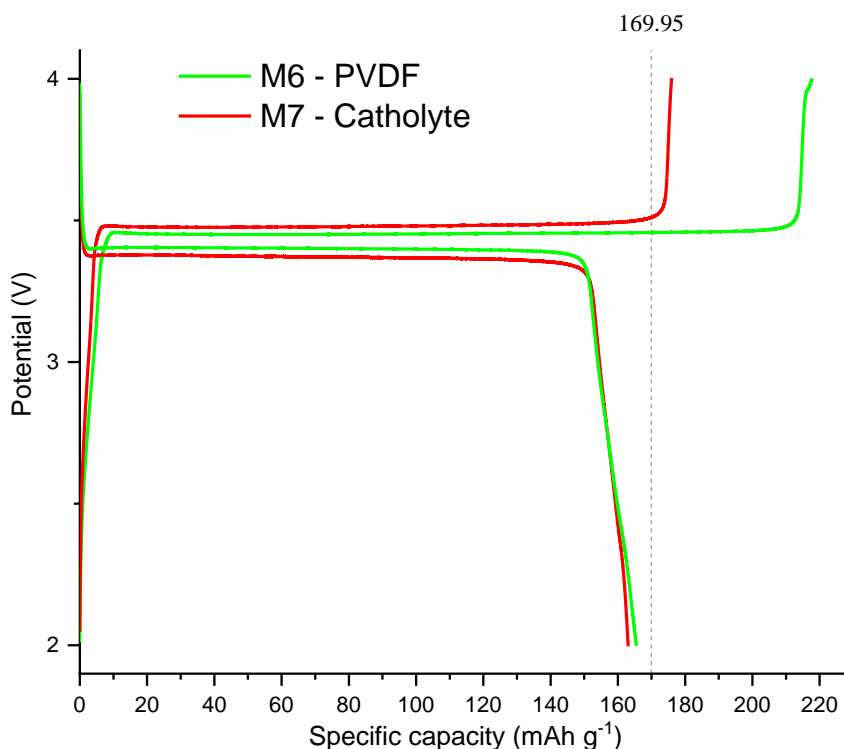
Figure 12. Voltage profiles of the third cycle at 0.1C of half-cells 6 and 7. Note that the charge curve for catholyte binder builds before the PVDF one.

Discharge curve remains unaltered as it is the resultant of a spontaneous electrochemical reaction, but the charge reaction is unspontaneous, and a voltage must be applied to force it. This strain increases the current load needed to attain the fully charged state. The catholyte offers less charge transport resistance for the Li^+ as it is designed to do so, thus decreasing discrepancies between charged and discharged states as the Coulombic efficiency approaches values up to ~95%.
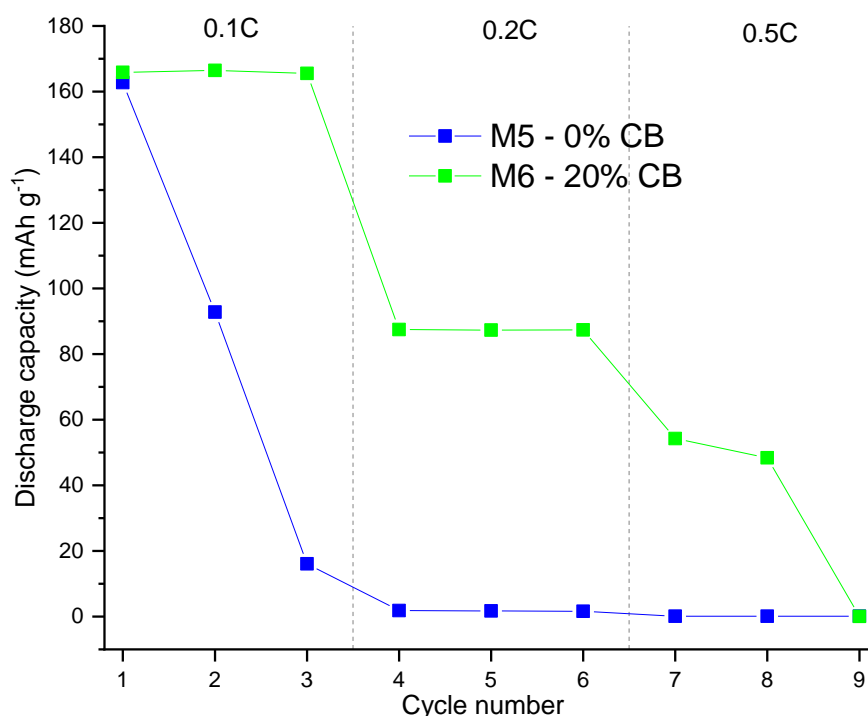
Figure 13. Discharge capacity vs. Cycle number at distinct C-rates. Note the steep capacity loss in the 0% CB sample.

Bad electronic conductivity of LFP material can be appreciated in **figure 13**. Electronic conductivity in the cathode is given by addition of extra CB. When it is not added, capacity fades upon the first cycles because of insulation of the cathode's bulk. LFP lithiation happens during its discharge process: Li^+ cations travel from the anode, through the electrolyte, and get reduced in the cathode by the electron coming from the Fe^{3+}/Fe^{2+} redox pair. Because $Fe^{III}PO_4$ is a poor electrical conductor, only the interphase of the cathode will reduce to $LiFe^{II}PO_4$, and the bulk will remain unreacted. Electrode polarization can also be observed when increasing C-rates. Capacity loss from 0.1C to 0.2C and to 0.5C is due to Li^+ building up in the cathode-electrolyte interphase because the insertion kinetics are slower than the rate at which the cations arrive. At high C-rates, electrostatic repulsions will finally take over and stop battery performance.

LFP@CB and solid electrolyte conditioning

Once the cathode performance with a LE was optimized, the same cathode was tested with a SE and specific capacity at 0.1C did not reach 0.1 mAh g^{-1} (**figure S29**). Interfacial contact of cathode-SE is one of the main issues with solid electrolytes. To improve it, one strategy is to increase the amount of catholyte in the cathode composition, so the two surfaces are more alike. Weight composition of the cathode was changed from 75:5:20 to 60:30:10 (LFP@CB:catholyte:CB) and specific discharged

capacity reached 0.3 mAh g^{-1} at 0.1C rate (**figure S30**). To improve the performance, different conditioning procedures before cycling the cells were tested. **Table 6** collects the conditionings tested. Once the battery is assembled, 'T-treatment' consisted in a thermal treatment of 70 ℃ for 15 hours. Second, 'P-treatment' is a pressure/thermal treatment in which the disassembled battery (the cathode|SE|Li sandwiched between SS collectors without the lids of the coin cell on) is heated at 70 ℃ while pressure is applied for 12 hours. After the P-treatment the cells was left to cool down, assembled and tested. Finally, 'P-internal' refers to the number of collectors inside the coin cell to increase the pressure contact within the battery elements.

Label	T-treatment	P-treatment	P-internal	Specific discharge capacities at 0.1C (mAh g^{-1})
C1	Yes	-	2	-
C2	-	140 g cm^{-2}	2	-
C3	-	30 g cm^{-2}	2	10-18
C4	Yes	-	3	99

Table 6. Specific discharge capacities at 0.1C for cathode|SE|Li cells with different conditioning treatments.

Upon cycling the C1 and C2 samples, current and voltage dropped to 0, respectively (**figure S31a and S31b**, respectively). Current drop in C1 was interpreted as result of electrode/electrolyte contact loss while cycling, although further experiments should be performed to have a clear explanation. Voltage drops in C2 meant the cell short-circuited. This was confirmed in C3 battery in which lower pressure was applied during heating and it did not short-circuit, although capacities were unimpressive. Interestingly, the capacity seemed to increase when many cycles at low C-rates were performed (**figure S32**). Some groups use this methodology to condition their batteries, but the process is very time consuming [29]. Internal pressure of 3 collectors was tested in C4 to maintain contact, and a thermal treatment was carried out to improve interfacial electrode-SE contact by "fusing" cathode and SE. It resulted in a specific discharge capacity of 99 mAh g^{-1} at 0.1C rate (**figure S33**) and settled the conditioning treatment.

Incorporation of LLZTO into the cathode – solid electrolyte system

The cathode composition remained in a 60:30:10 ratio for LFP@CB : catholyte : CB and the catholyte, in turn, had a 30 wt% of LLZTO ceramic material. As explained in 'Solid electrolyte membrane preparation', two ceramic composite electrolytes were studied whose only difference was the amount of solvent: 7 mL or 10 mL of AcN (LLZ-7 and LLZ-10 electrolytes, respectively). Both electrolyte compositions were incorporated as catholyte into separated cathodes, which were labelled as Z7 and Z10. Z7 cells were tested with T-treatment, P-treatment, and P-internal of 2 and 3 collectors, and the highest capacity reached was ~6 mAh g^{-1}. On the other hand, Z10 conditioned with a T-treatment reached capacities up to 99 mAh g^{-1}. These differences can be attributed to microstructure. Highest porosity of Z7 can be appreciated in the profile SEM images in **figure 14**. Both cathodes' thickness is around 10 µm.
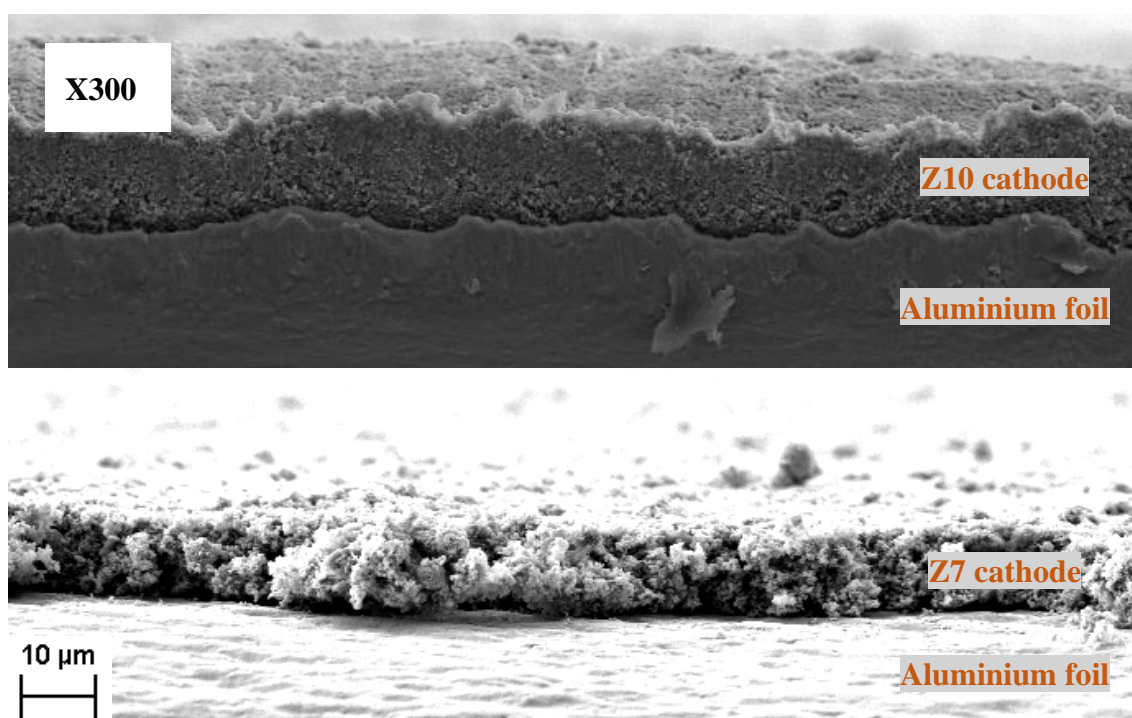
Figure 14. Profile SEM images at 10 kV. Both cathodes have similar thickness but Z10 (a) is more compact than Z7 (b)

As **figure 15** shows, addition of the ceramic material greatly enhances stability of the cathode. C4 sample shows appreciable damages in stability and loss of capacity from the third cycle. Nonetheless, Z10 maintains stability and seems to improve its capacity upon cycling. Each charge/discharge cycle lasts around 8 hours, therefore studying deep cycling for more than 10 cycles was not possible because of the availability of the experimental equipment. The ceramic material also improved cyclability and lowered

polarizability of the cell. As evidenced in **figure 16**, 0.2C rate can be supported by Z10 and it still reaches 50 mAh g^{-1} with coulombic efficiencies around 100%, while the polarizability effect in C4 is too high and capacity fades.
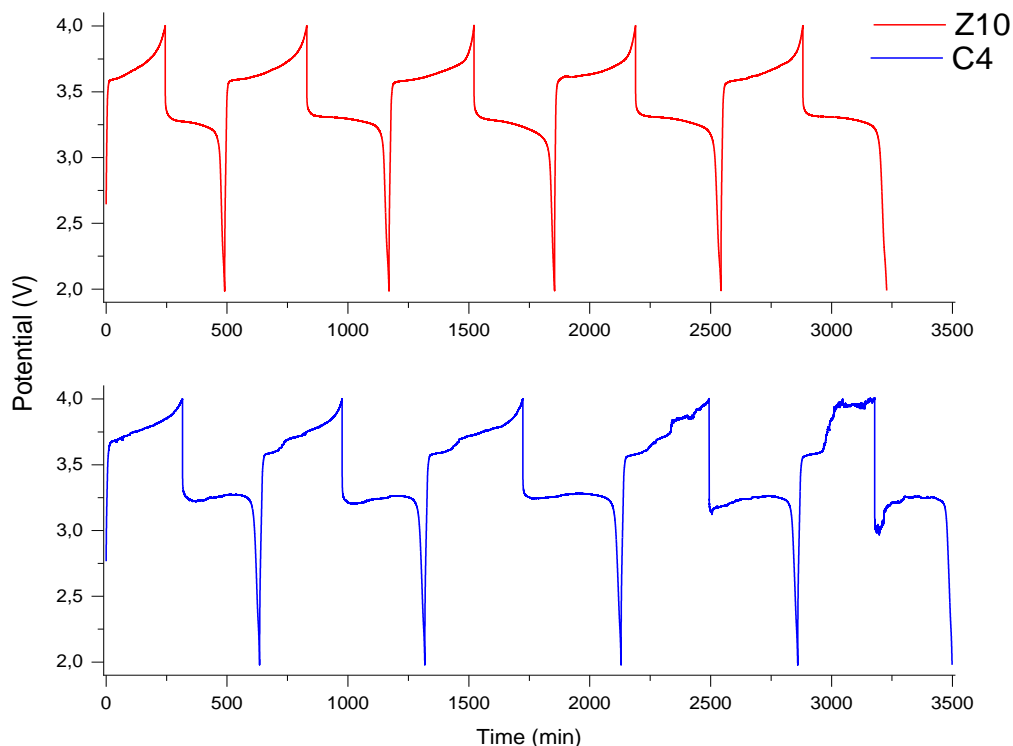
Figure 15. Potential vs time profiles showing 5 cycles at 0.1C rate during charge/discharge. The presence of LLZTO in Z10 stabilizes the cell upon cycling.
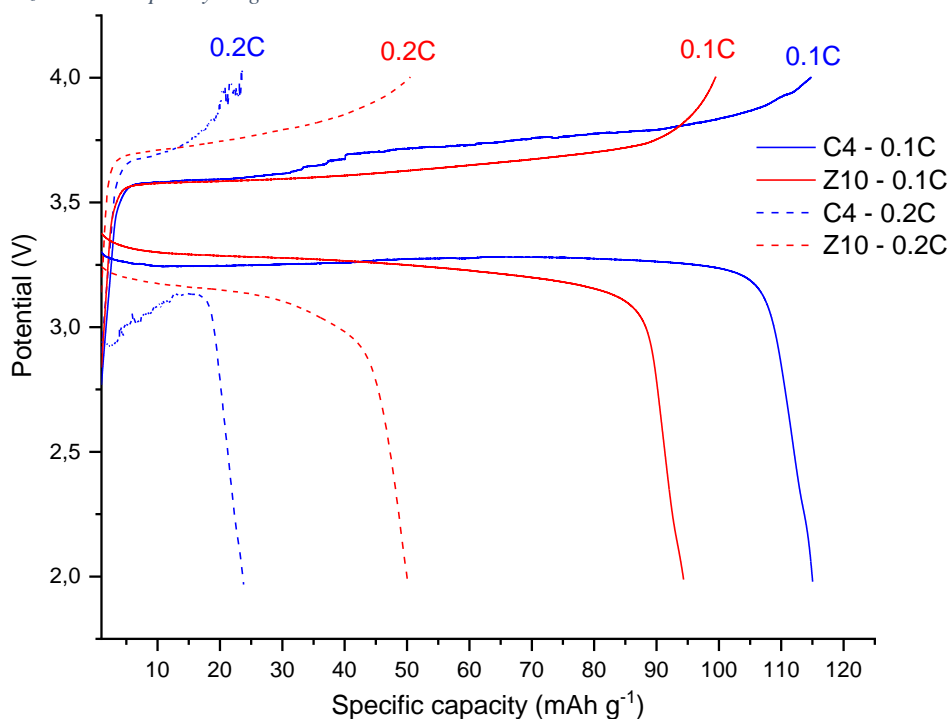
Figure 16. Voltage profiles of the third cycles for C4 and Z10 samples at 0.1C and 0.2C show huge improvements in polarizability by addition of LLZTO.

5. CONCLUSIONS

There are substantial changes afoot in the generation and storage of energy. The prospects that the climate crisis predicts, and depletion of non-renewable natural resources for power generation, prompt research on green and renewable energy generation, together with sustainable, safe, and efficient storage. Solar cell and wind turbines, among others, are accountable for energy extraction. Depending on the amount and future use of the generated energy, different storage approaches are created. Transforming electrical into potential energy in dams would solve the problem of intermittent sources, where immense amounts of energy are generated with no control of time/demand. Lithium-ion batteries are still the selected technology for portable electronics such as laptops, mobile phones, relatively small medical devices, etc. But the energy density (in weight or volume) provided by elemental lithium anodes is determinant for other applications as the electric vehicle. The drawbacks of lithium anodes have been discussed in the introduction, and to palliate them a solid electrolyte have been tested in solid-state-batteries.

The main objectives of this work have been successfully achieved: synthesis and characterization of a composite solid electrolyte, a cathode whose composition contains catholyte to improve the interphase in the fully assembled cells, and several conditioning procedures developed. The final result is sample Z10, with enhanced cyclability and polarization.

There is still room for improvement. Polarization is too high for large power demands and the cathode voltage can be upgraded by modifying its composition and/or structure. Cyclability should have been checked in more depth (remember that 30,000 cycles are ahead of a battery with 10 years of operational life), but the specific equipment was not yet there at the time this work was done.

Finally, research on solid-state-batteries is a huge field with so many open windows. I believe the protocols established in this work will speed up the exploration of this large topic in the department.

BIBLIOGRAPHY

[1]   A. Yoshino, "The birth of the lithium-ion battery," *Angewandte Chemie - International Edition*, vol. 51, no. 24. pp. 5798–5800, Jun. 11, **2012**. doi: 10.1002/anie.201105006.

[2]   N. Nitta, F. Wu, J. T. Lee, and G. Yushin, "Li-ion battery materials: Present and future," *Materials Today*, vol. 18, no. 5. Elsevier B.V., pp. 252–264, Jun. 01, **2015**. doi: 10.1016/j.mattod.2014.10.040.

[3]   J. B. Goodenough and K. S. Park, "The Li-ion rechargeable battery: A perspective," *Journal of the American Chemical Society*, vol. 135, no. 4. pp. 1167–1176, Jan. 30, **2013**. doi: 10.1021/ja3091438.

[4]   H.-J. Kim, B.-S. Jin, C.-H. Doh, and H.-S. Kim, "Electrochemical Properties and Thermal Stability of LiNi 0.8 Co 0.15 Al 0.05 O 2 -LiFePO 4 Mixed Cathode Materials for Lithium Secondary Batteries ," *Journal of Electrochemical Science and Technology*, vol. 3, no. 2, pp. 63–67, Jun. **2012**, doi: 10.5229/jecst.2012.3.2.63.

[5]   J. B. Goodenough and Y. Kim, "Challenges for rechargeable Li batteries," *Chemistry of Materials*, vol. 22, no. 3. pp. 587–603, Feb. 09, **2010**. doi: 10.1021/cm901452z.

[6]   X. H. Rui, Y. Jin, X. Y. Feng, L. C. Zhang, and C. H. Chen, "A comparative study on the low-temperature performance of LiFePO 4/C and Li3V2(PO4)3/C cathodes for lithium-ion batteries," *Journal of Power Sources*, vol. 196, no. 4, pp. 2109–2114, Feb. **2011**, doi: 10.1016/j.jpowsour.2010.10.063.

[7]   E. Paled, "The Electrochemical Behavior of Alkali and Alkaline Earth Metals in Nonaqueous Battery Systems-The Solid Electrolyte Interphase Model." **1979**, doi: 10.1149/1.2128859

[8]   D. Lin, Y. Liu, and Y. Cui, "Reviving the lithium metal anode for high-energy batteries," *Nature Nanotechnology*, vol. 12, no. 3. Nature Publishing Group, pp. 194–206, Mar. 07, **2017**. doi: 10.1038/nnano.2017.16.

[9]   K. Huang, Z. Li, Q. Xu, H. Liu, H. Li, and Y. Wang, "Lithiophilic CuO Nanoflowers on Ti-Mesh Inducing Lithium Lateral Plating Enabling Stable Lithium-Metal Anodes with Ultrahigh Rates and Ultralong Cycle Life," *Advanced Energy Materials*, vol. 9, no. 29, Aug. **2019**, doi: 10.1002/aenm.201900853.

[10]   C. Brissot, M. Rosso, J.-N. Chazalviel, S. Lascaud, and F. Francè´, "Dendritic growth mechanisms in lithiumrpolymer cells." **1999**, doi: 10.1016/S0378-7753(98)00242-0

[11]   Z. Zhang, Y. Huang, H. Gao, J. Huang, C. Li, and P. Liu, "An all-solid-state lithium battery using the Li7La3Zr2O12 and Li6.7La3Zr1.7Ta0.3O12 ceramic enhanced polyethylene oxide electrolytes with superior electrochemical performance," *Ceramics International*, vol. 46, no. 8, pp. 11397–11405, Jun. **2020**, doi: 10.1016/j.ceramint.2020.01.170.

[12]   F. Chen *et al.*, "Solid polymer electrolytes incorporating cubic Li7La3Zr2O12 for all-solid-state lithium rechargeable batteries," *Electrochimica Acta*, vol. 258, pp. 1106–1114, Dec. **2017**, doi: 10.1016/j.electacta.2017.11.164.

[13]   E. Bekaert, L. Buannic, U. Lassi, A. Llordés, and J. Salminen, "Chapter one - Electrolytes for Li- and Na-Ion Batteries: Concepts, Candidates, and the Role of Nanotechnology," **2017**. doi: 10.1016/B978-0-323-42977-1/00001-7.

[14]   Mikrajudding Abdullah, Wuled Lenggoro, and Kikuo Okuyama, *Polymer Electrolyte Nanocomposites*. American Scientific Publishers, **2004**.

[15]   S. B. Aziz, T. J. Woo, M. F. Z. Kadir, and H. M. Ahmed, "A conceptual review on polymer electrolytes and ion transport models," *Journal of Science: Advanced Materials and Devices*, vol. 3, no. 1. Elsevier B.V., pp. 1–17, Mar. 01, **2018**. doi: 10.1016/j.jsamd.2018.01.002.

[16]   L. Chen, Y. Li, S. P. Li, L. Z. Fan, C. W. Nan, and J. B. Goodenough, "PEO/garnet composite electrolytes for solid-state lithium batteries: From 'ceramic-in-polymer' to

'polymer-in-ceramic,'" *Nano Energy*, vol. 46, pp. 176–184, Apr. **2018**, doi: 10.1016/j.nanoen.2017.12.037.

[17] K. Pan *et al.*, "A Flexible Ceramic/Polymer Hybrid Solid Electrolyte for Solid-State Lithium Metal Batteries," *Advanced Materials*, vol. 32, no. 17, Apr. **2020**, doi: 10.1002/adma.202000399.

[18] H. Buschmann *et al.*, "Structure and dynamics of the fast lithium-ion conductor 'li 7La3Zr2O12,'" *Physical Chemistry Chemical Physics*, vol. 13, no. 43, pp. 19378–19392, Nov. **2011**, doi: 10.1039/c1cp22108f.

[19] V. Wurster, C. Engel, H. Graebe, T. Ferber, W. Jaegermann, and R. Hausbrand, "Characterization of the Interfaces in LiFePO 4 /PEO-LiTFSI Composite Cathodes and to the Adjacent Layers ," *Journal of The Electrochemical Society*, vol. 166, no. 3, pp. A5410–A5420, **2019**, doi: 10.1149/2.0621903jes.

[20] W. Zaman, N. Hortance, M. B. Dixit, V. de Andrade, and K. B. Hatzell, "Visualizing percolation and ion transport in hybrid solid electrolytes for Li-metal batteries," *Journal of Materials Chemistry A*, vol. 7, no. 41, pp. 23914–23921, **2019**, doi: 10.1039/c9ta05118j.

[21] Nuria Vicente i Agut. "Design, Synthesis, and Characterization of New Generation Lithium Batteries". Ph.D. Dissertation, Escola de Doctorat de la Universitat Jaume I, **2019**.

[22] K. Funke and R. D. Banhatti, "Ionic motion in materials with disordered structures," *Solid State Ionics*, vol. 177, no. 19-25 SPEC. ISS., pp. 1551–1557, Oct. **2006**, doi: 10.1016/j.ssi.2005.12.037.

[23] D. K. Pradhan, R. N. P. Choudhary, and B. K. Samantaray, "Studies of dielectric and electrical properties of plasticized polymer nanocomposite electrolytes," *Materials Chemistry and Physics*, vol. 115, no. 2–3, pp. 557–561, Jun. **2009**, doi: 10.1016/j.matchemphys.2009.01.008.

[24] S. Lascaud, M. Perrier, A. Vallke, S. Besner, J. Prud'homme, and M. Armand, "Phase Diagrams and Conductivity Behavior of Poly(ethy1ene oxide)-Molten Salt Rubbery Electrolytes," **1994**. doi: 10.1021/ma00103a034

[25] G. Guzmán, J. Vazquez-Arenas, G. Ramos-Sánchez, M. Bautista-Ramírez, and I. González, "Improved performance of LiFePO4 cathode for Li-ion batteries through percolation studies," *Electrochimica Acta*, vol. 247, pp. 451–459, Sep. **2017**, doi: 10.1016/j.electacta.2017.06.172.

[26] K. M. Abraham, Z. Jiang, and B. Carroll, "Highly Conductive PEO-like Polymer Electrolytes," **1997**. doi: 10.1021/cm970075a

[27] A. Gutiérrez-Pardo *et al.*, "Will the competitive future of solid-state Li metal batteries rely on a ceramic or a composite electrolyte?" *Sustainable Energy and Fuels*, vol. 2, no. 10, pp. 2325–2334, **2018**, doi: 10.1039/c8se00273h.

[28] A. J. Bard and L. R. Faulkner, *Electrochemical methods: fundamentals and applications*.

[29] Z. Wan *et al.*, "Low Resistance–Integrated All-Solid-State Battery Achieved by Li7La3Zr2O12 Nanowire Upgrading Polyethylene Oxide (PEO) Composite Electrolyte and PEO Cathode Binder," *Advanced Functional Materials*, vol. 29, no. 1, Jan. **2019**, doi: 10.1002/adfm.201805301.

[30] W. Goreckit, M. Jeannint, E. Belorizkyt, C. Roux$, and M. Armand, "Physical properties of solid polymer electrolyte PEO(LiTFSI) complexes," **1995**. doi: 10.1088/0953-8984/7/34/007

[31] V. Wenzel, H. Nirschl, and D. Nötzel, "Challenges in Lithium-Ion-Battery Slurry Preparation and Potential of Modifying Electrode Structures by Different Mixing Processes," *Energy Technology*, vol. 3, no. 7, pp. 692–698, Jul. **2015**, doi: 10.1002/ente.201402218.

APPENDICES

Confocal microscopy images.

Every confocal microscopy sample was supported on top a Mylar sheet, therefore 0.77 µm must be extracted to the measured thickness.
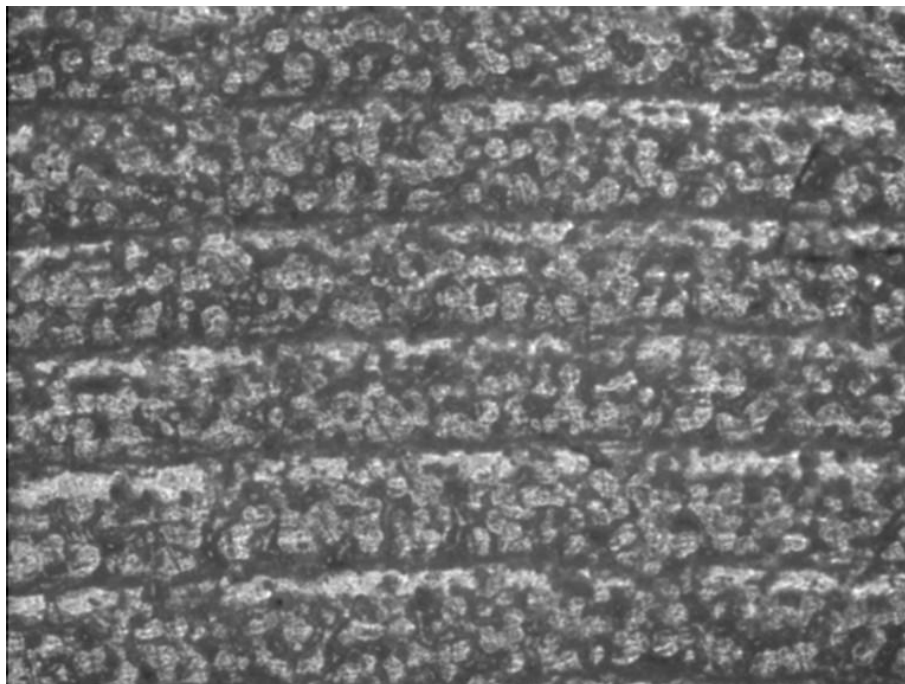
Supplementary figure 1. Optical image from the REF solid electrolyte surface. The wave-like pattern corresponds to the machining in the teflon petri dishes.
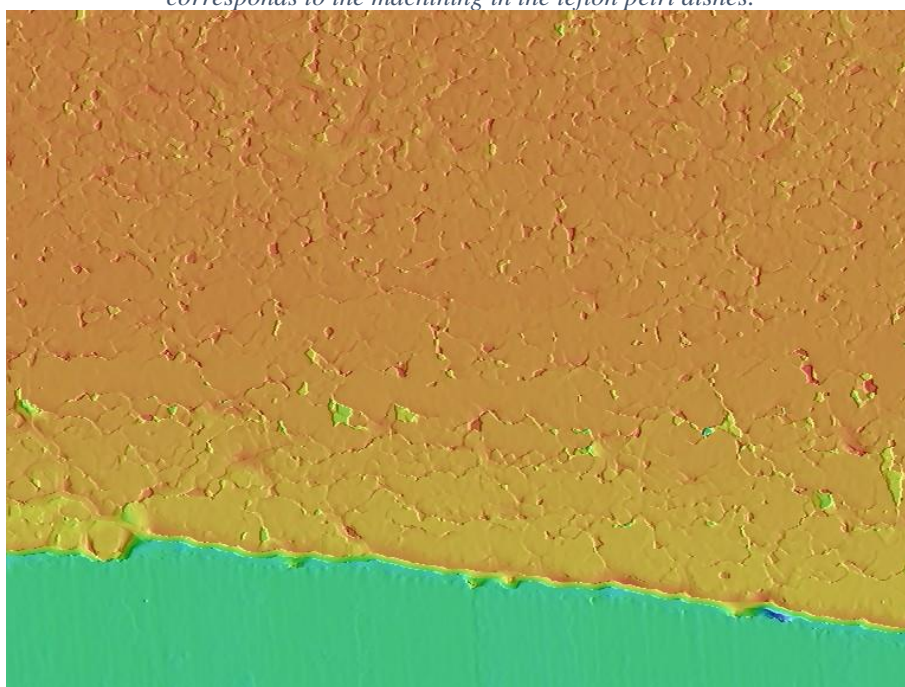
Supplementary figure 2. Surface of REF solid electrolyte (x10). Sample was cut with scissors.
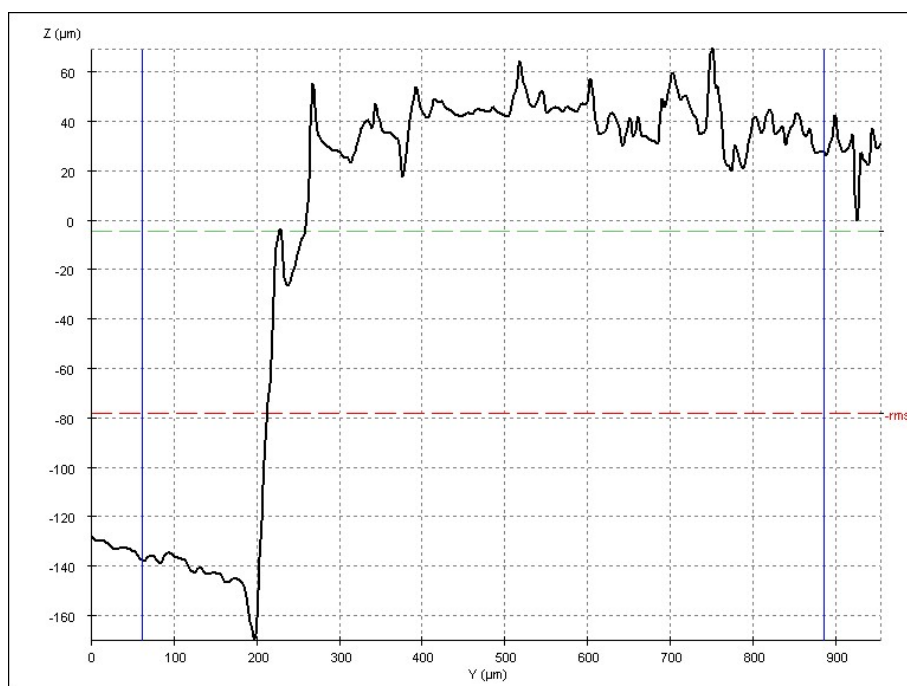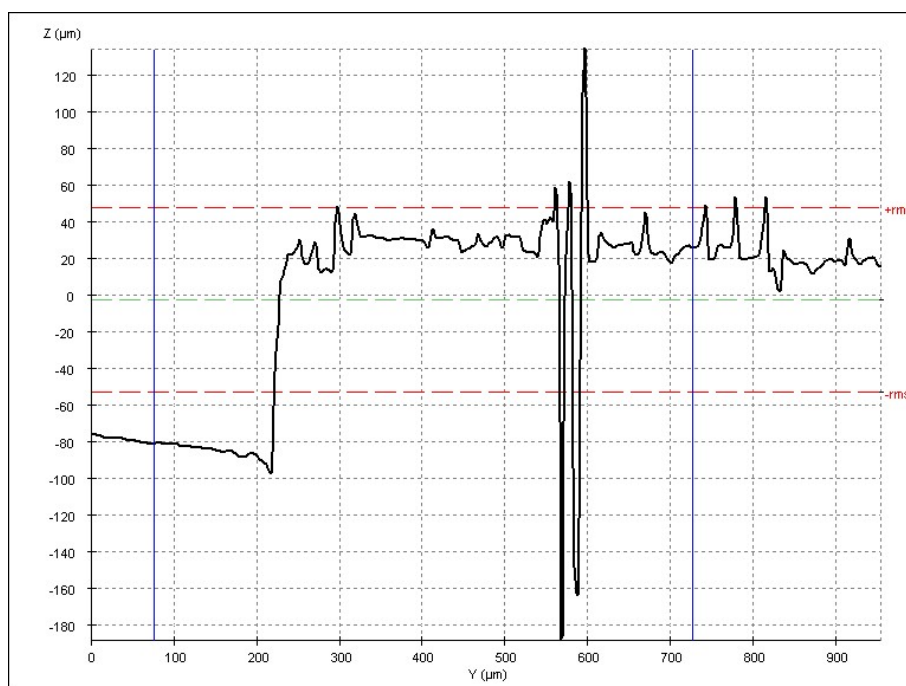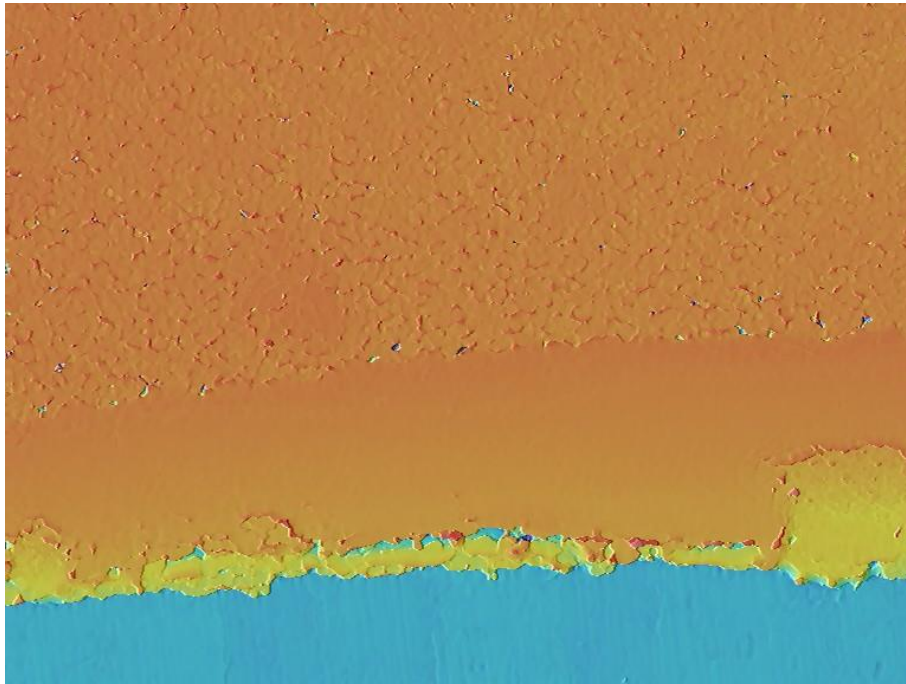
Supplementary figure 3. Profile of REF solid electrolyte.
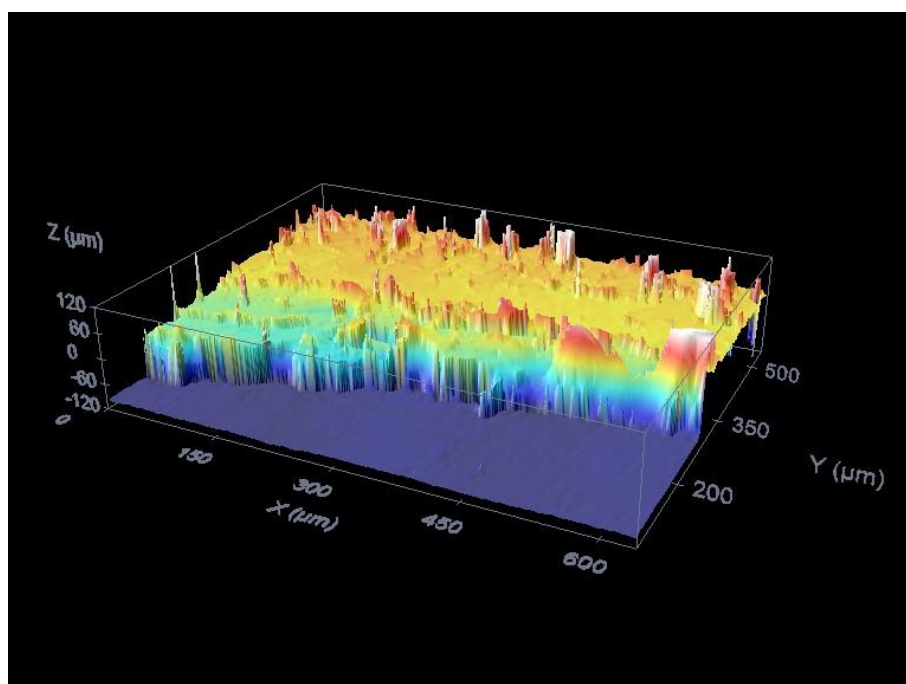
Supplementary figure 4. 3D reproduction of electrolyte LLZ-10.
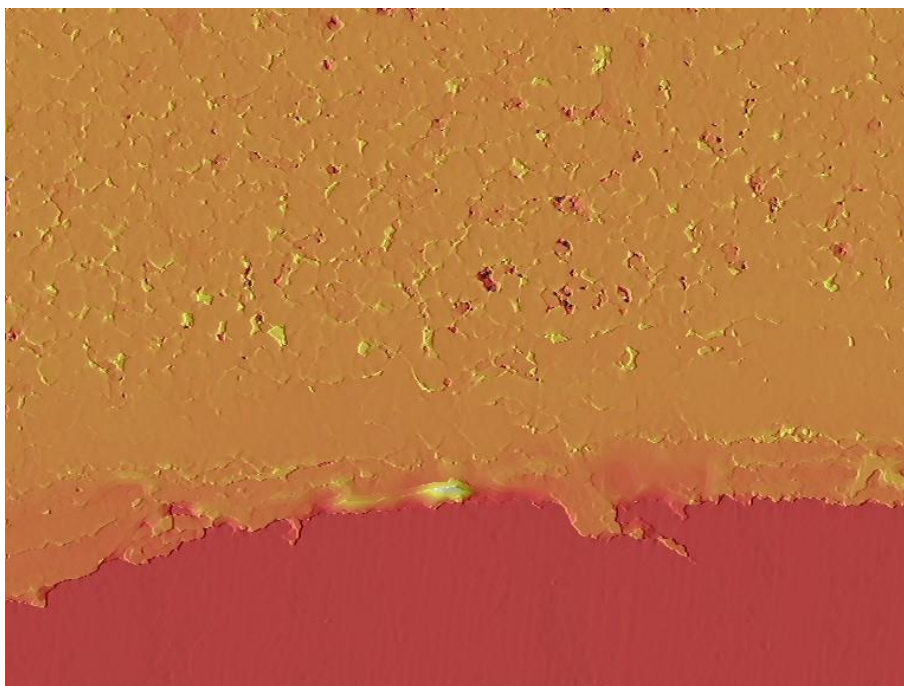
Supplementary figure 5. Surface of LLZ-10 solid electrolyte (x10). Sample was cut with scissors.

Supplementary figure 6. Profile of LLZ-10 solid electrolyte. Impossibilities appear at Y ~580 µm, they will not be acknowledged in future figures.

Supplementary figure 7. Surface of LLZ-7 (x10). Sample was cut with the 15-mm cylindrical puncher used to cut every SE.
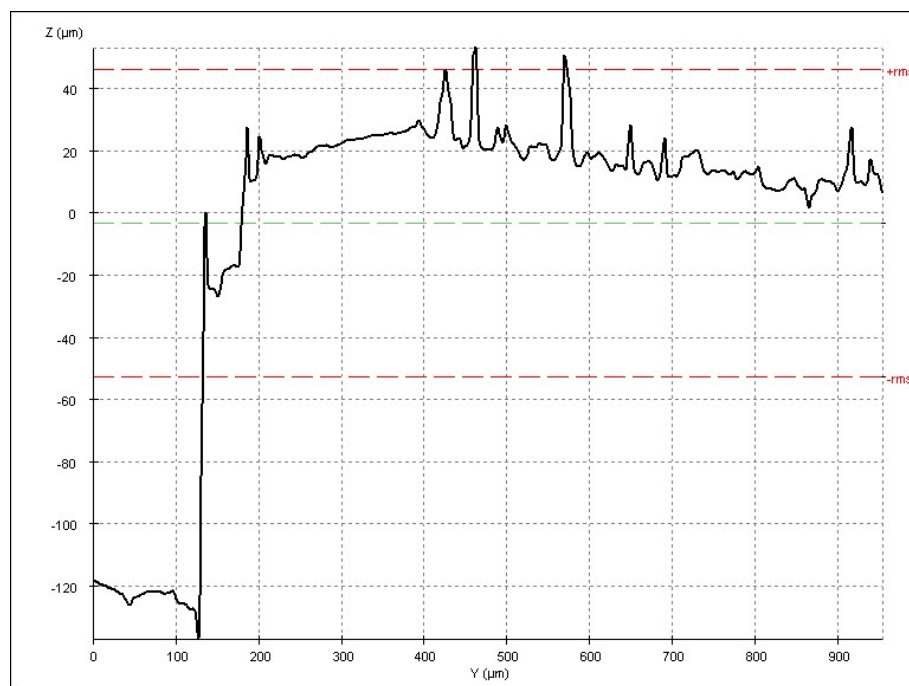
Supplementary figure 8. Profile of LLZ-7.

DSC curves.
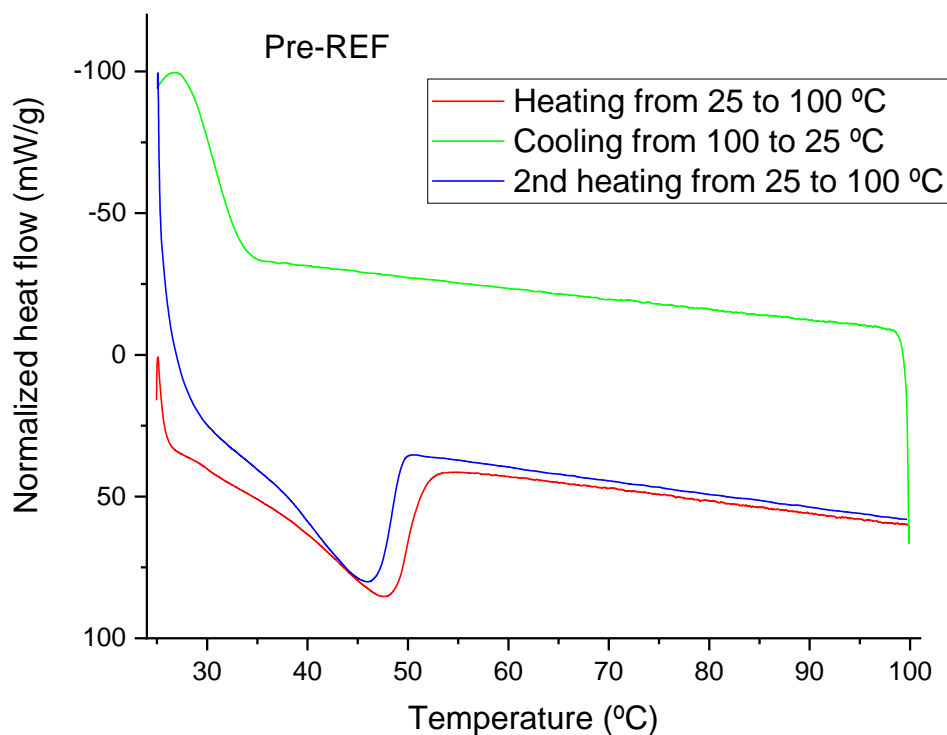
Supplementary figure 9. Electrolyte Pre-REF curves of normalized heat flow vs temperature.
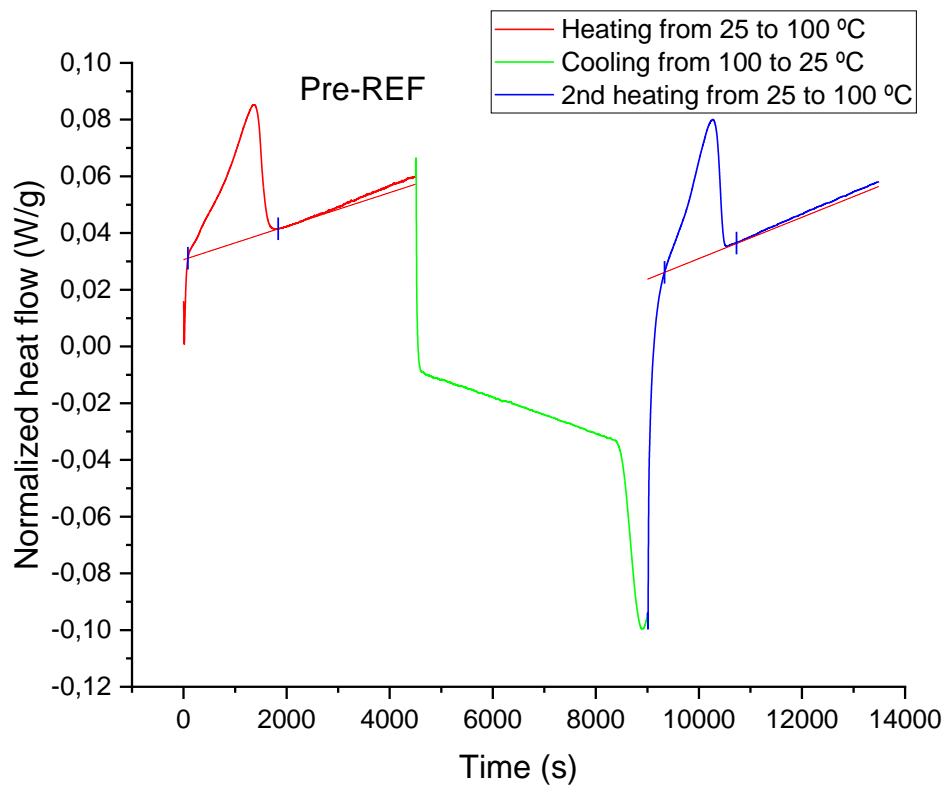
Supplementary figure 10. Electrolyte Pre-REF curves of normalized heat flow vs time. Baseline indicating the area under the curve used to calculate ΔH$_f$ and crystallinity is showed.
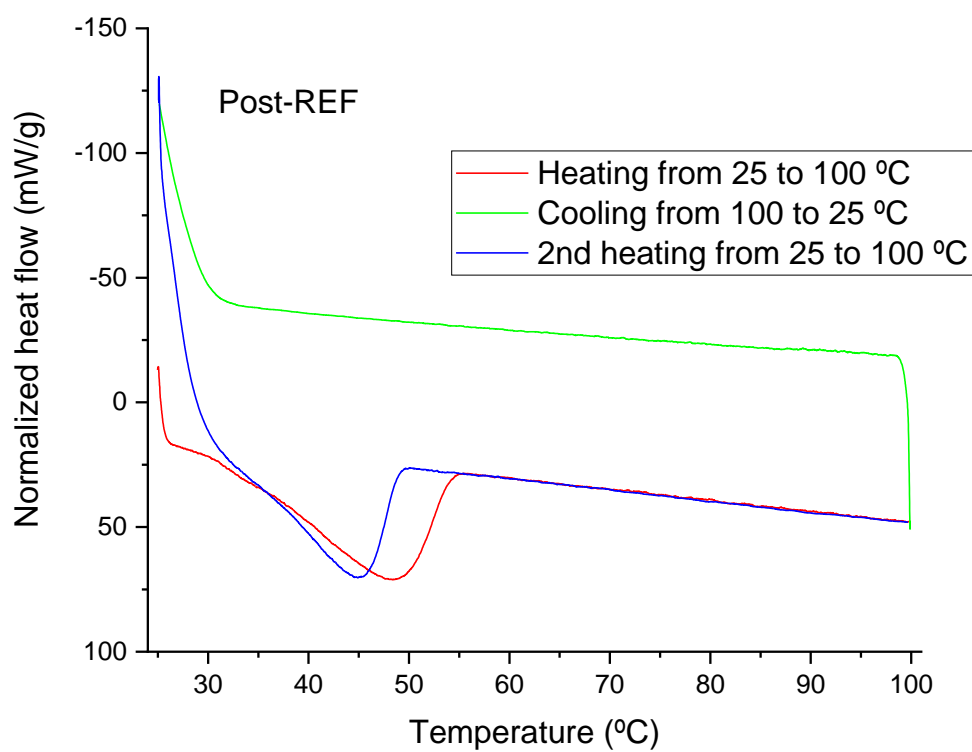
Supplementary figure 11. Electrolyte Post-REF curves of normalized heat flow vs temperature.
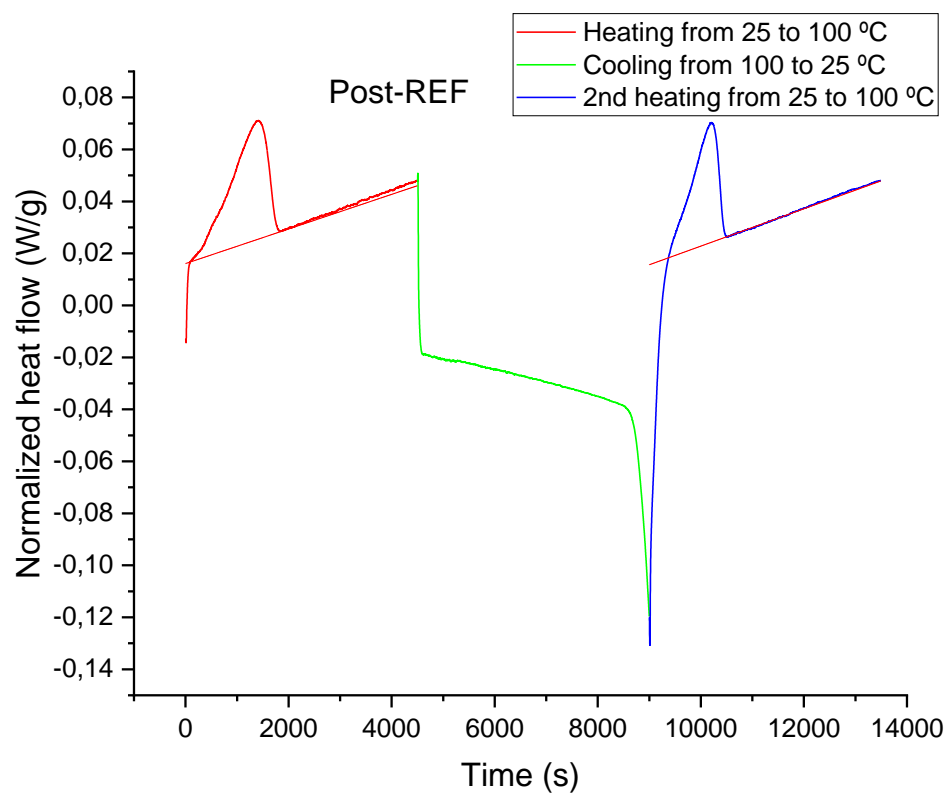
Supplementary figure 12. Electrolyte Post-REF curves of normalized heat flow vs time. Baseline indicating the area under the curve used to calculate ΔH_f and crystallinity is showed.
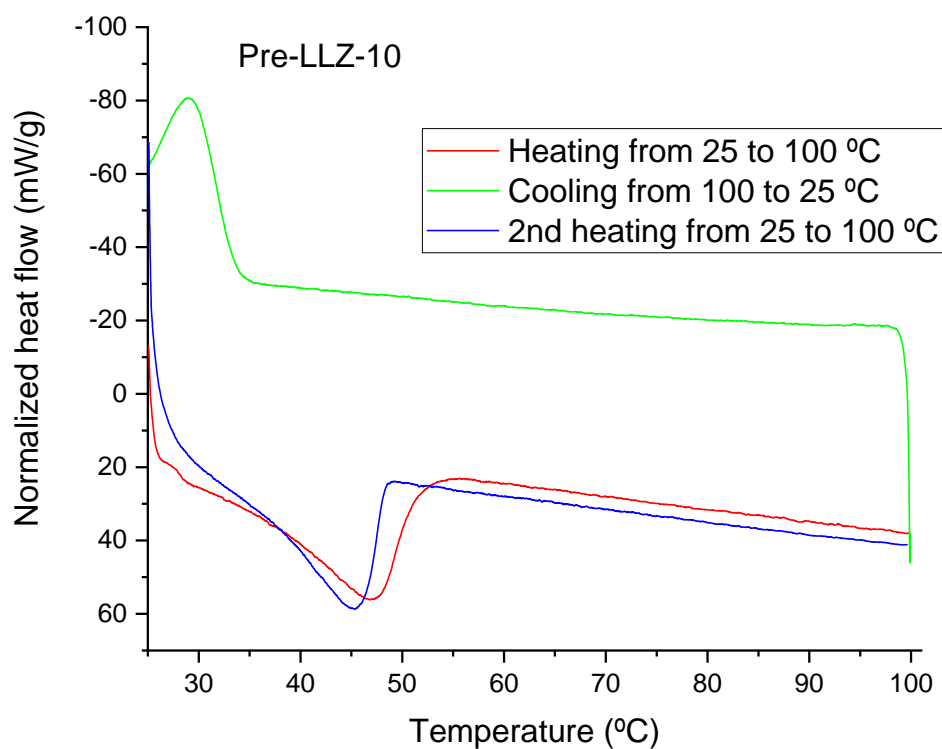
Supplementary figure 13. Electrolyte Pre-LLZ-10 curves of normalized heat flow vs temperature.
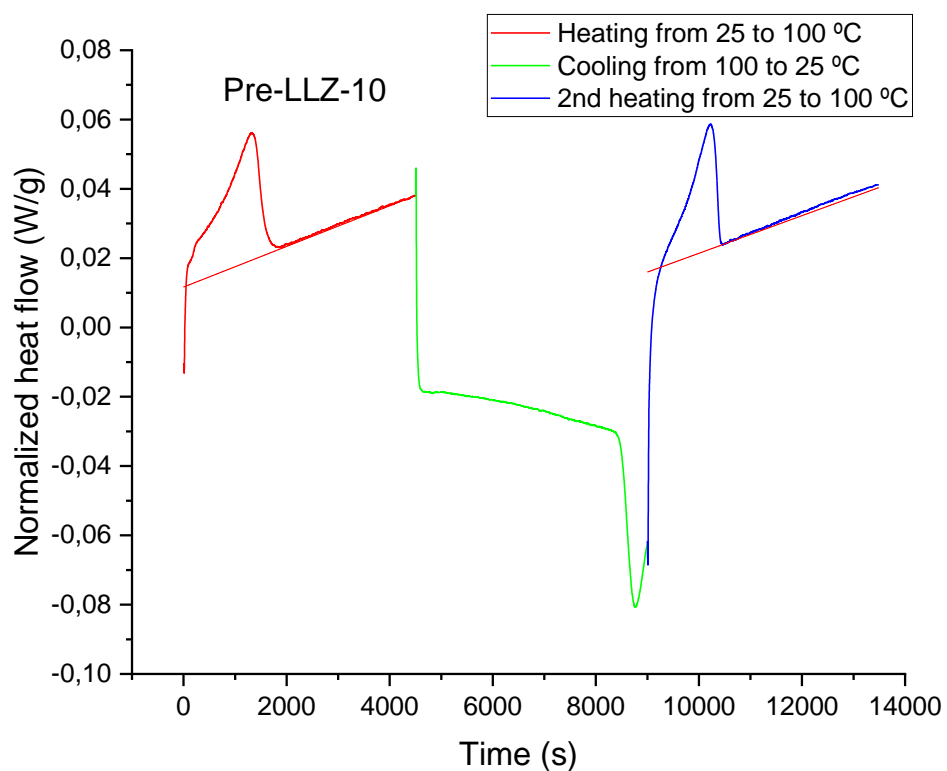
Supplementary figure 14. Electrolyte Pre-LLZ-10 curves of normalized heat flow vs time. Baseline indicating the area under the curve used to calculate ΔH_f and crystallinity is showed.
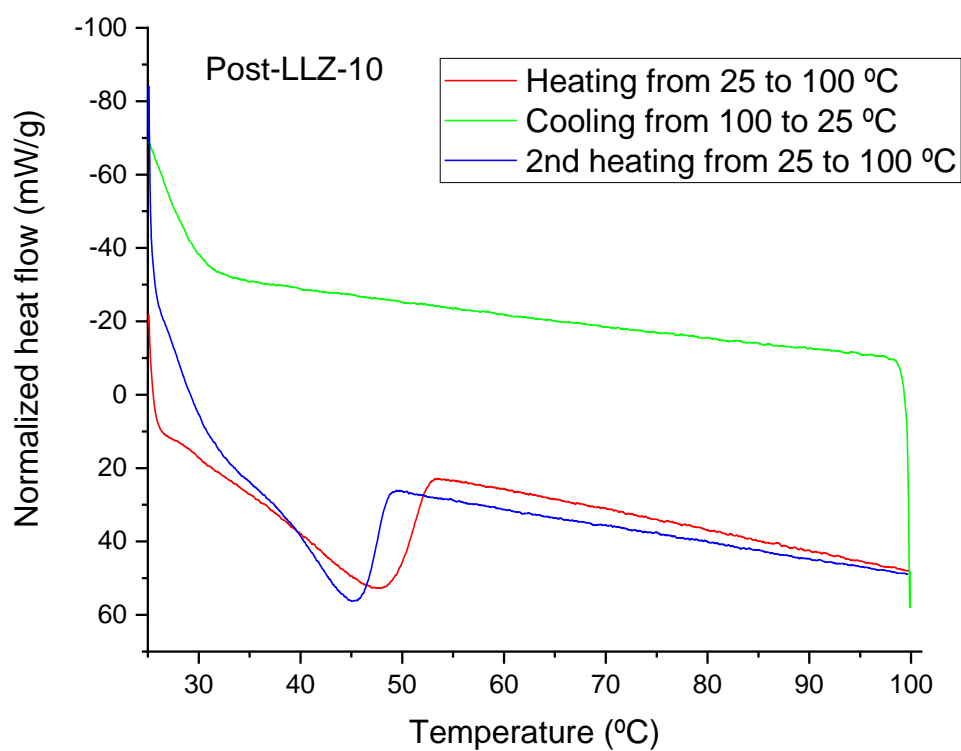
Supplementary figure 15. Electrolyte Pre-LLZ-10 curves of normalized heat flow vs temperature.
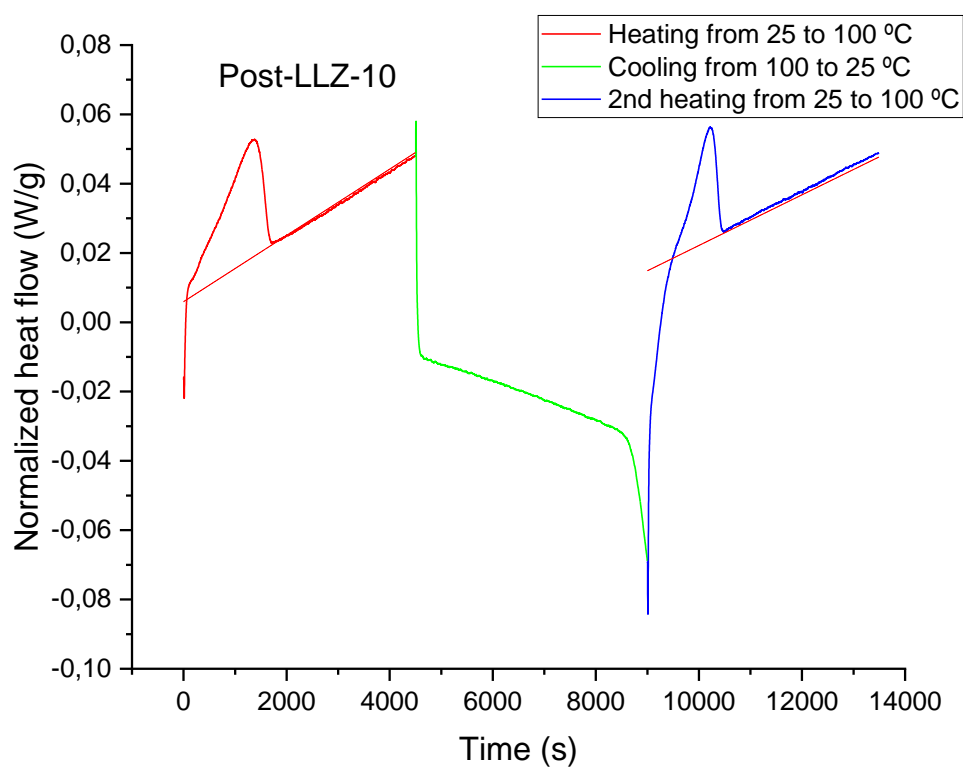
Supplementary figure 16. Electrolyte Post-LLZ-10 curves of normalized heat flow vs time. Baseline indicating the area under the curve used to calculate ΔH$_f$ and crystallinity is showed.

TGA.
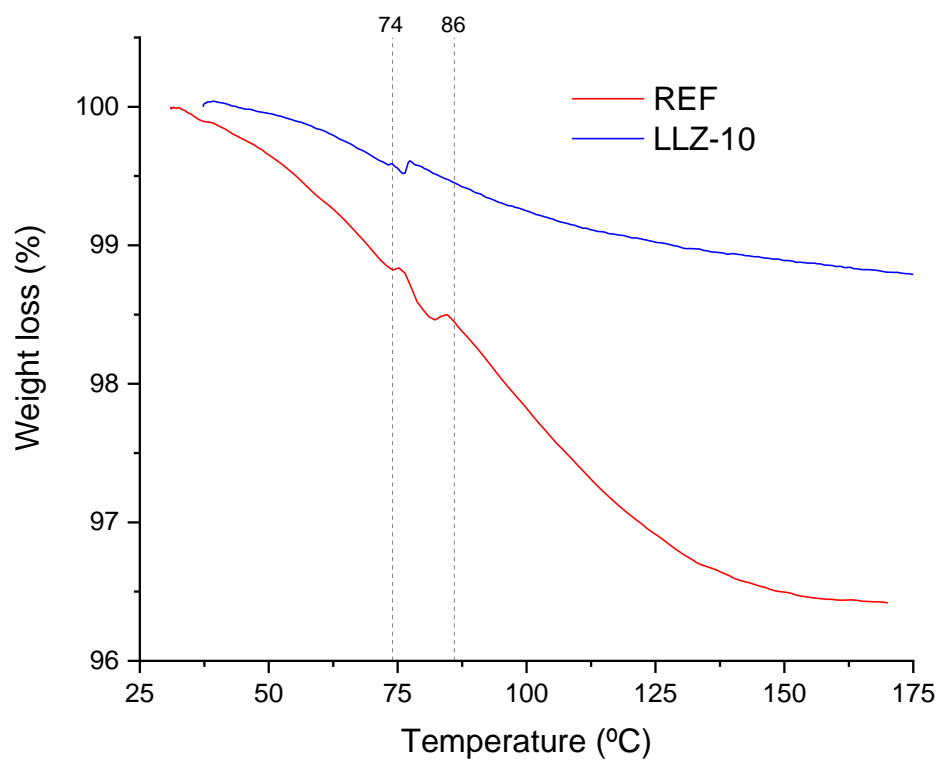
Supplementary figure 17. Curve from 25 to 175 ºC show peaks between 74 and 86 ºC probably corresponding to acetonitrile's boiling point. Constant weight loss may indicate hydration of the samples.

Ionic conductivity measurements.
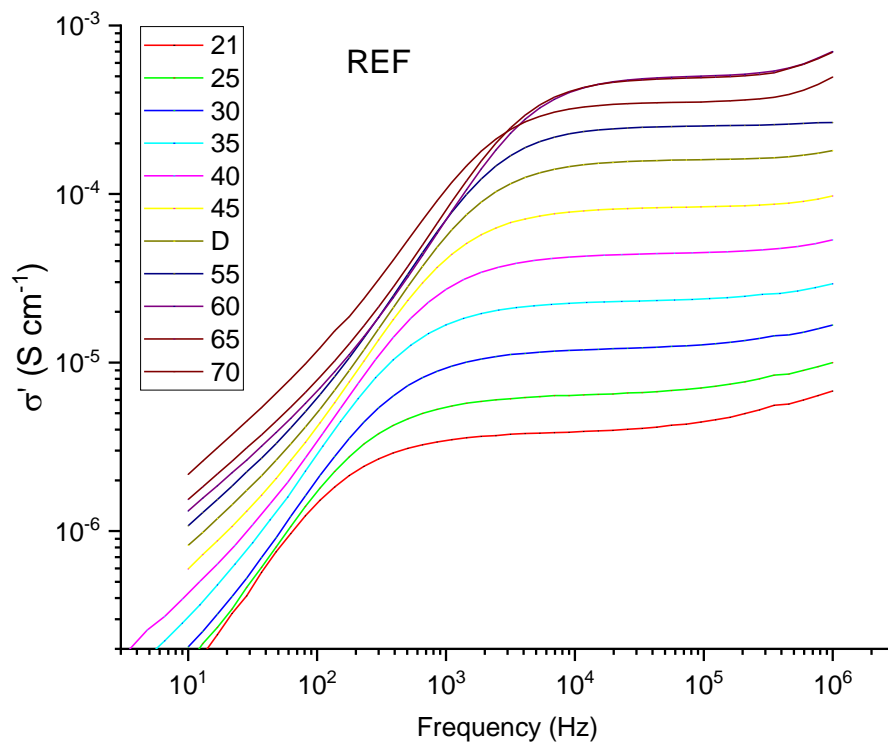
Supplementary figure 18. Real conductivity vs Frequency for REF electrolyte. The plateau region is the value of ionic conductivity at each temperature.
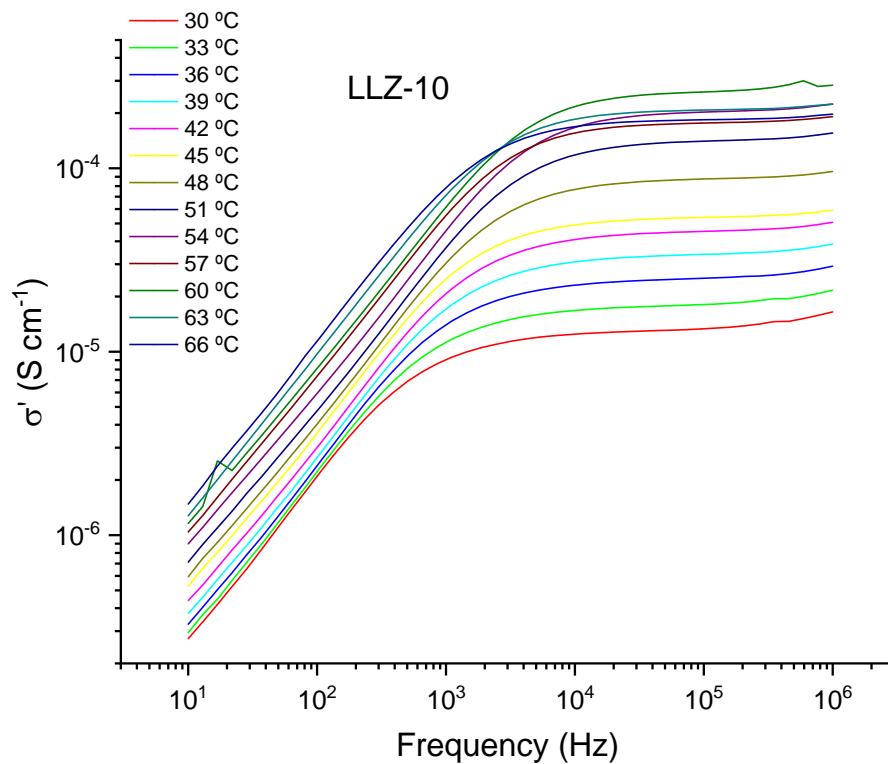
Supplementary figure 19. Real conductivity vs. Frequency for LLZ-10 electrolyte. The plateau region is the value of ionic conductivity at each temperature.

Transport number measurements.
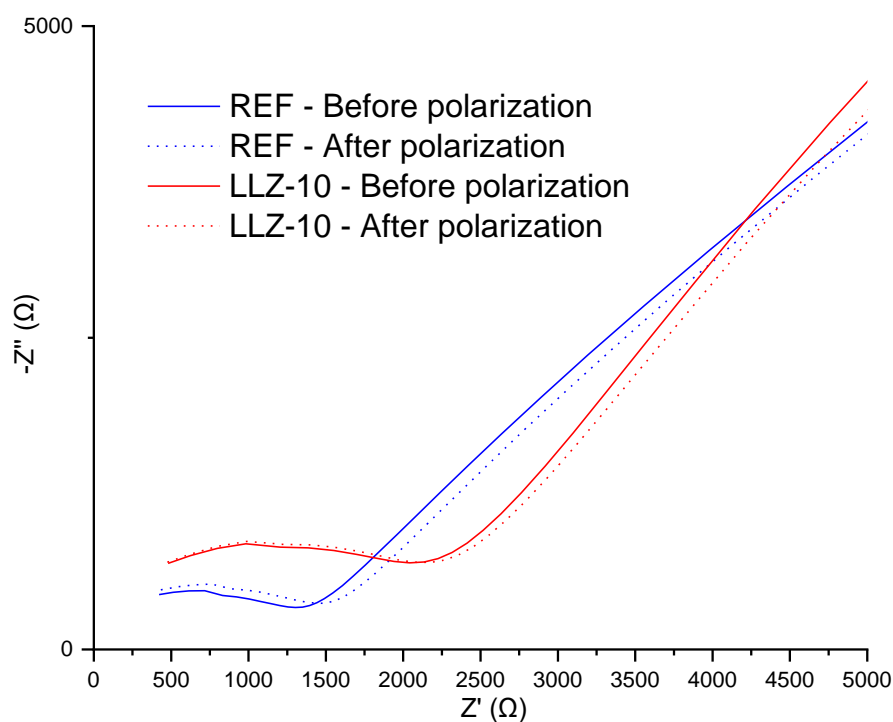
Supplementary figure 20. EIS Nyquist plots. Increase in resistance due to the apparition of a passivation layer in the electrode-electrolyte interface during polarization by chronoamperometry at 10 mV.
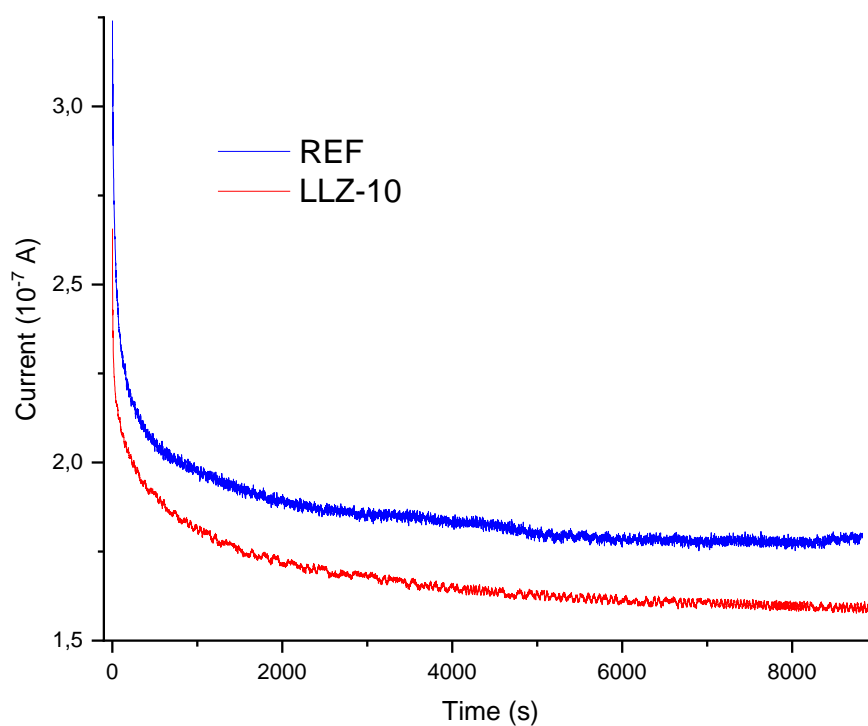
Supplementary figure 21. Chronoamperometry at 10 mV triggers a concentration gradient that affects mobility of the ions and reduces the current circulating through the electrolyte until a steady state.

Cycling experiments.
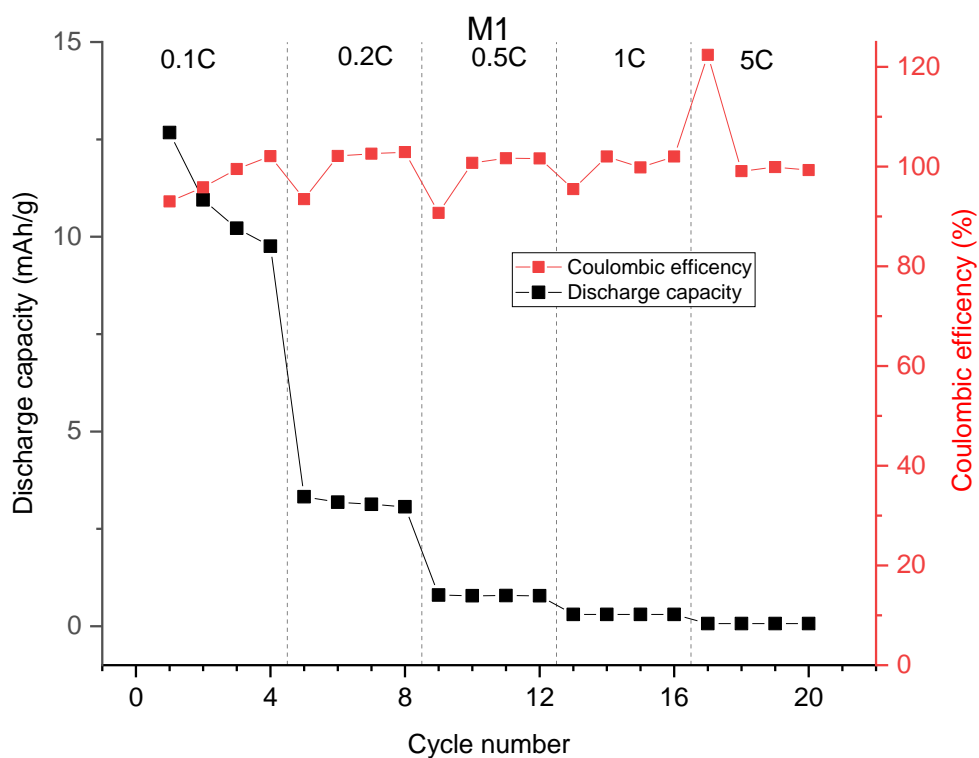
Supplementary figure 22. Cycling of battery M1.
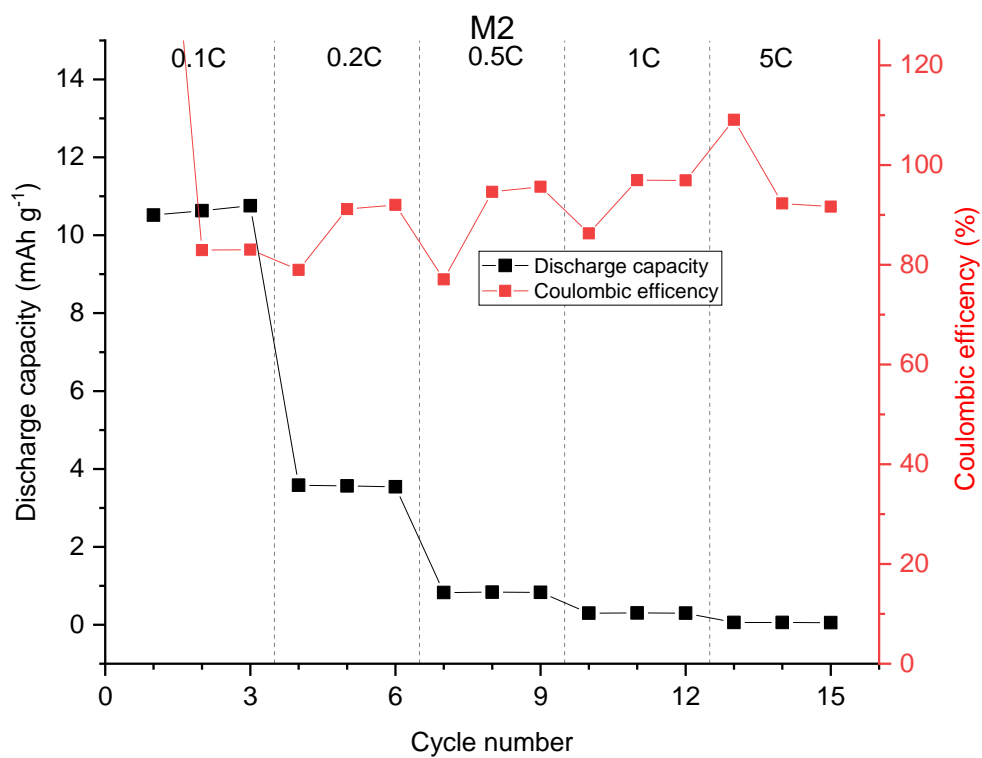
Supplementary figure 23. Cycling of battery M2.
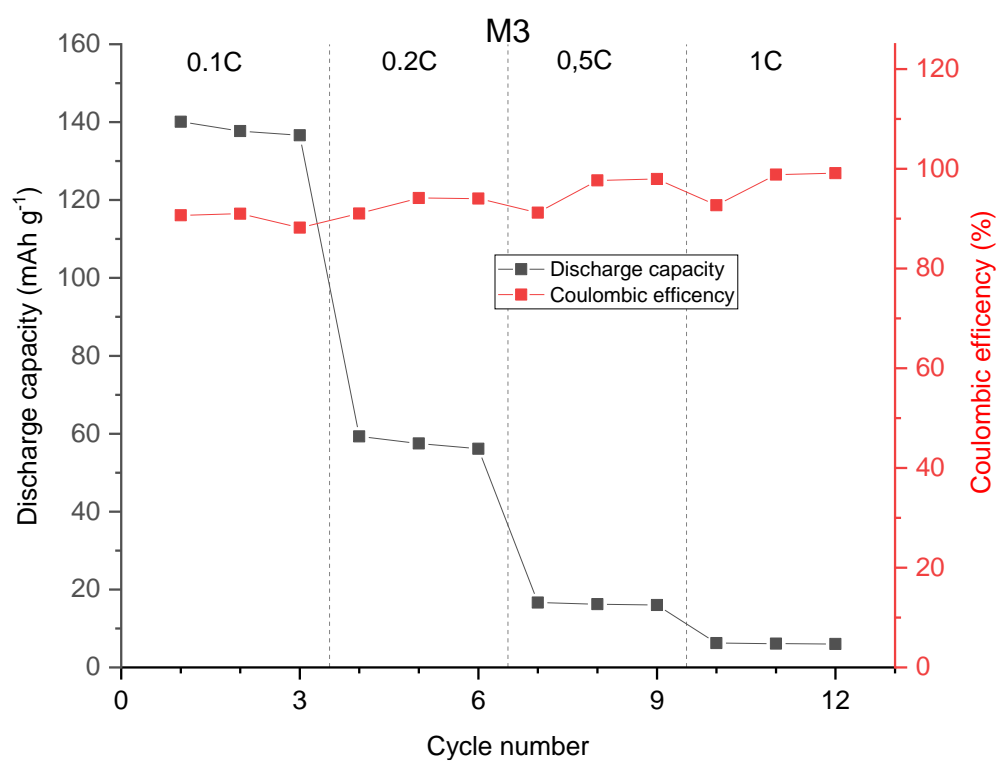
Supplementary figure 24. Cycling of battery M3.
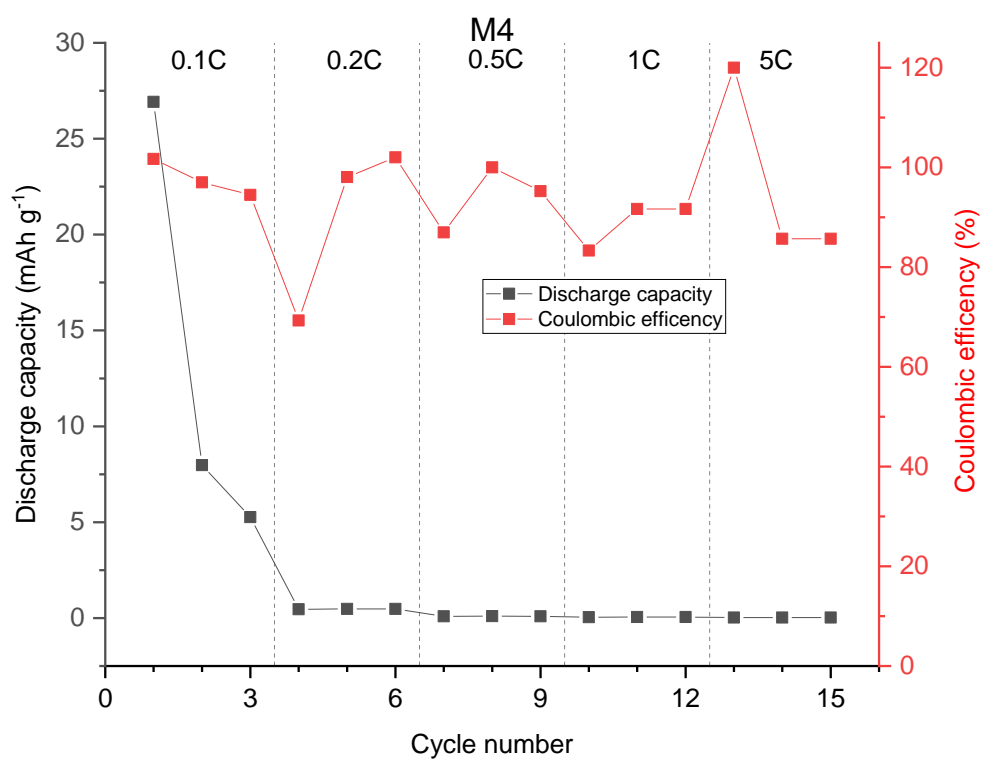
Supplementary figure 25. Cycling of battery M4.
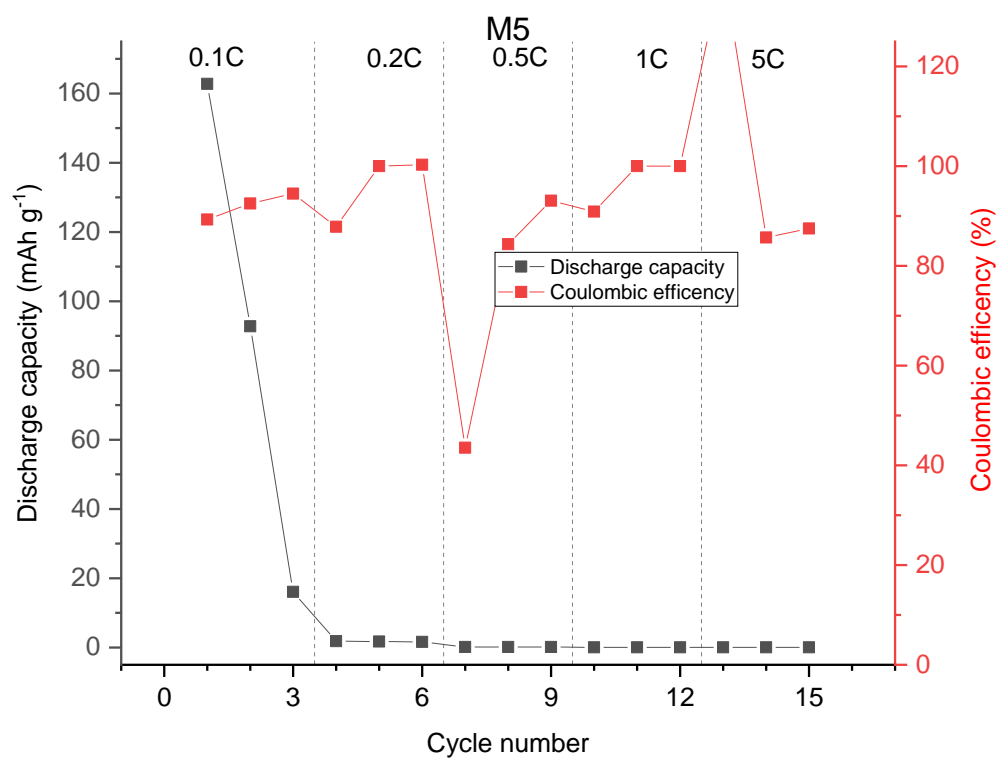
Supplementary figure 26. Cycling of battery M5.
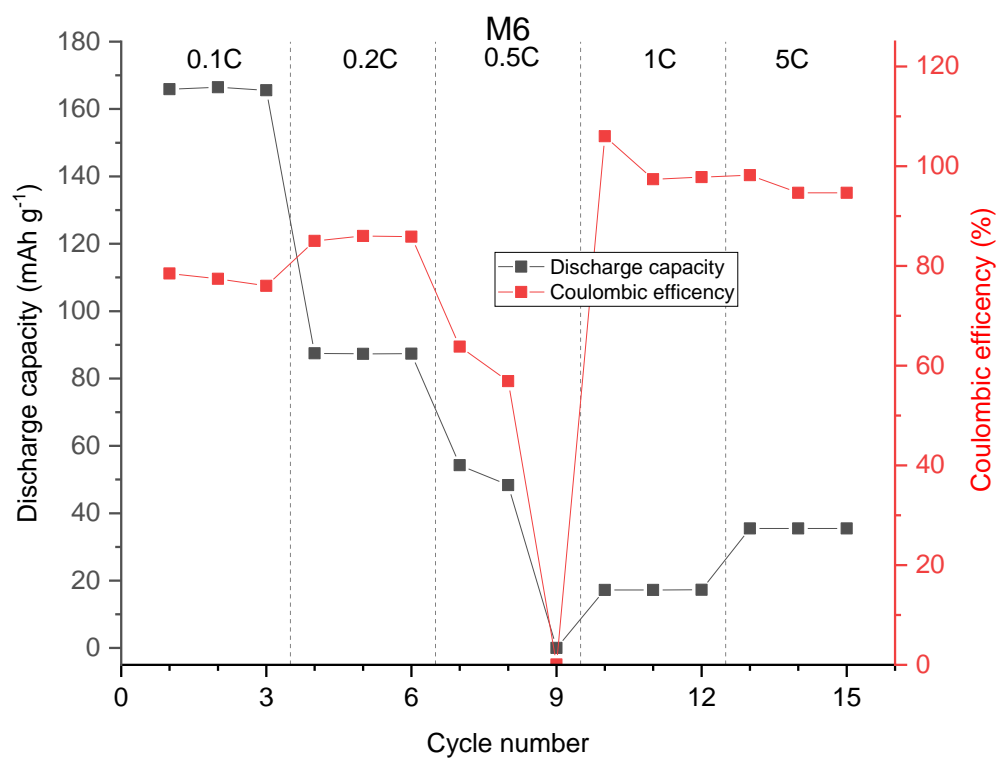
Supplementary figure 27. Cycling of battery M6.
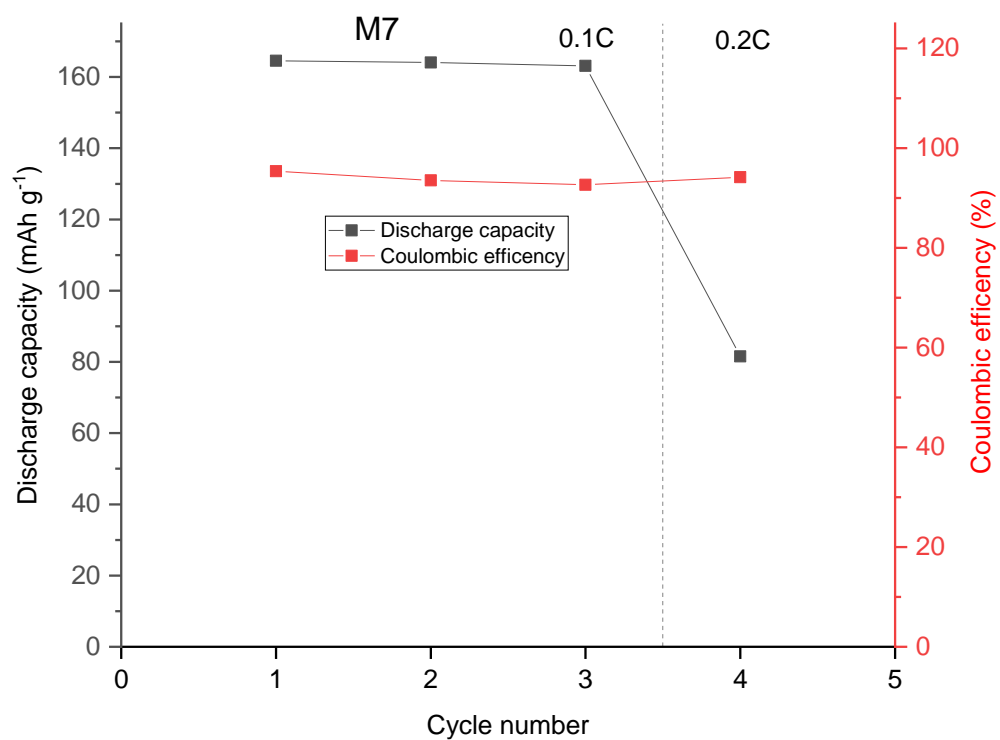
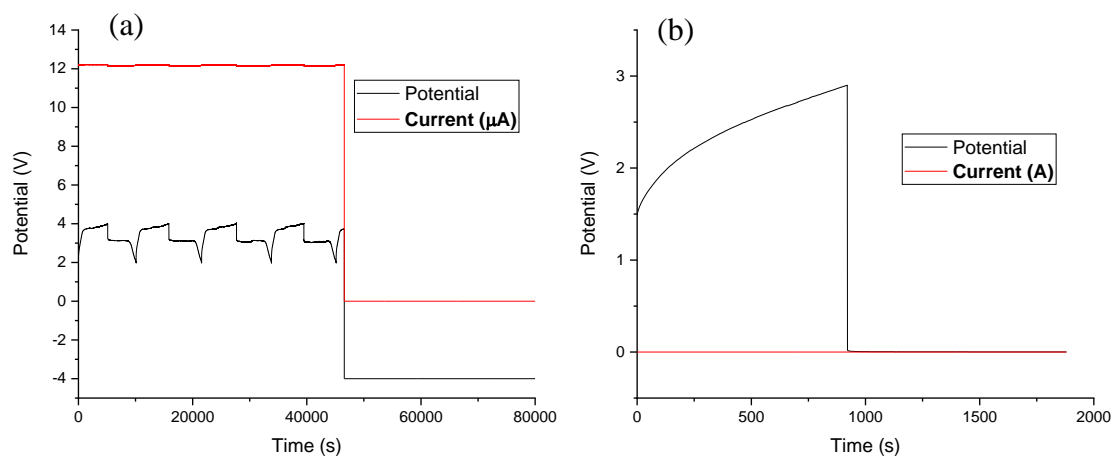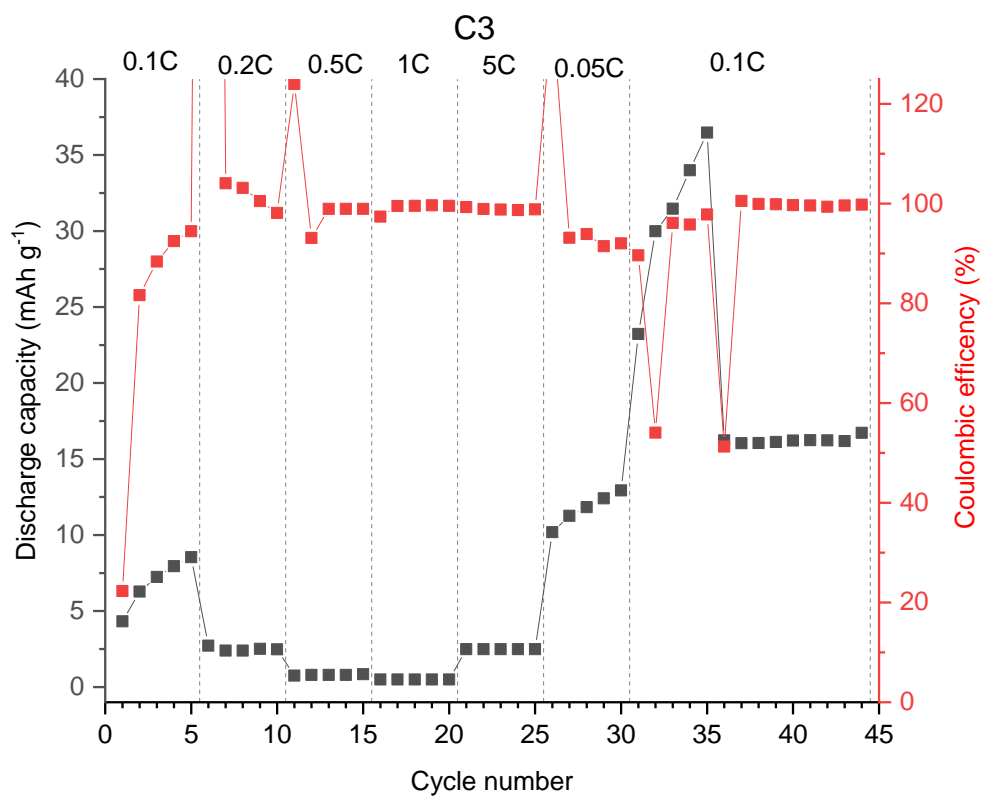*Supplementary figure 28. Cycling of battery M7.*
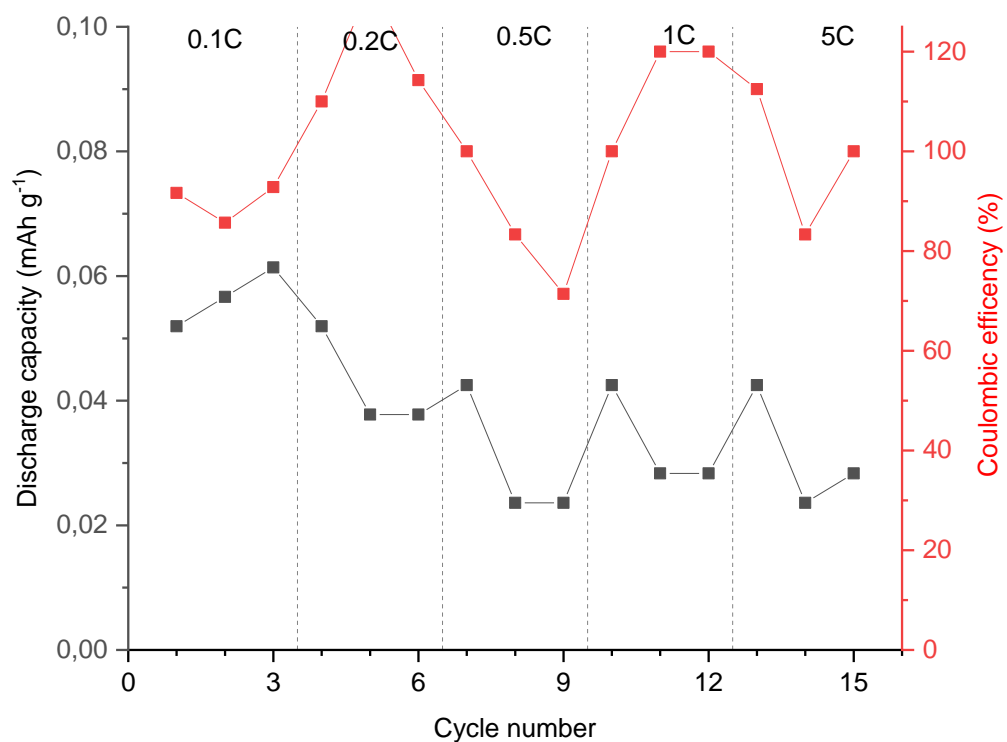
Supplementary figure 29. Incorporation of solid electrolyte without conditioning. Composition: 75:5:20 of LFP@CB:catholyte:CB.
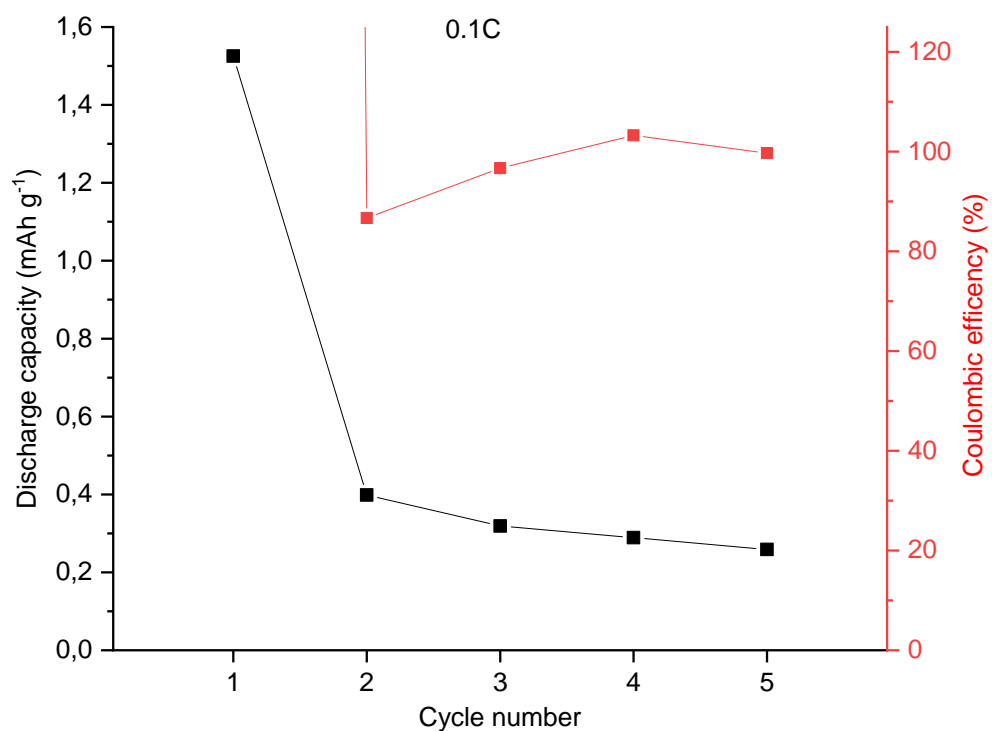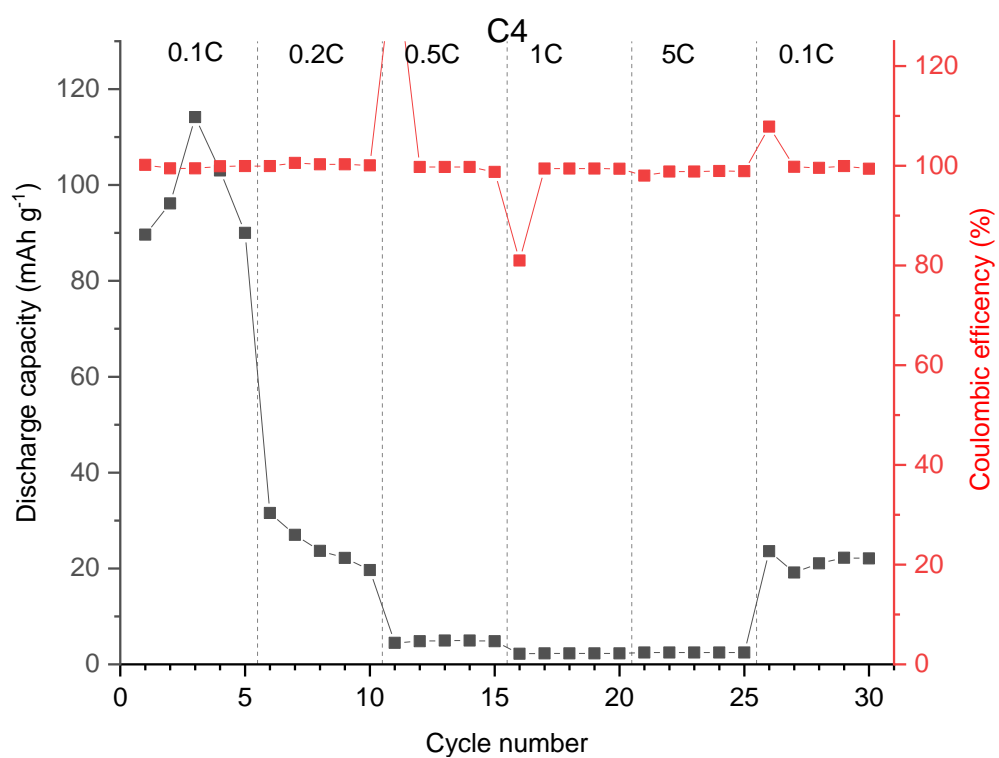
Supplementary figure 30. Incorporation of solid electrolyte without conditioning. Composition: 60:30:10 of LFP@CB:catholyte:CB.
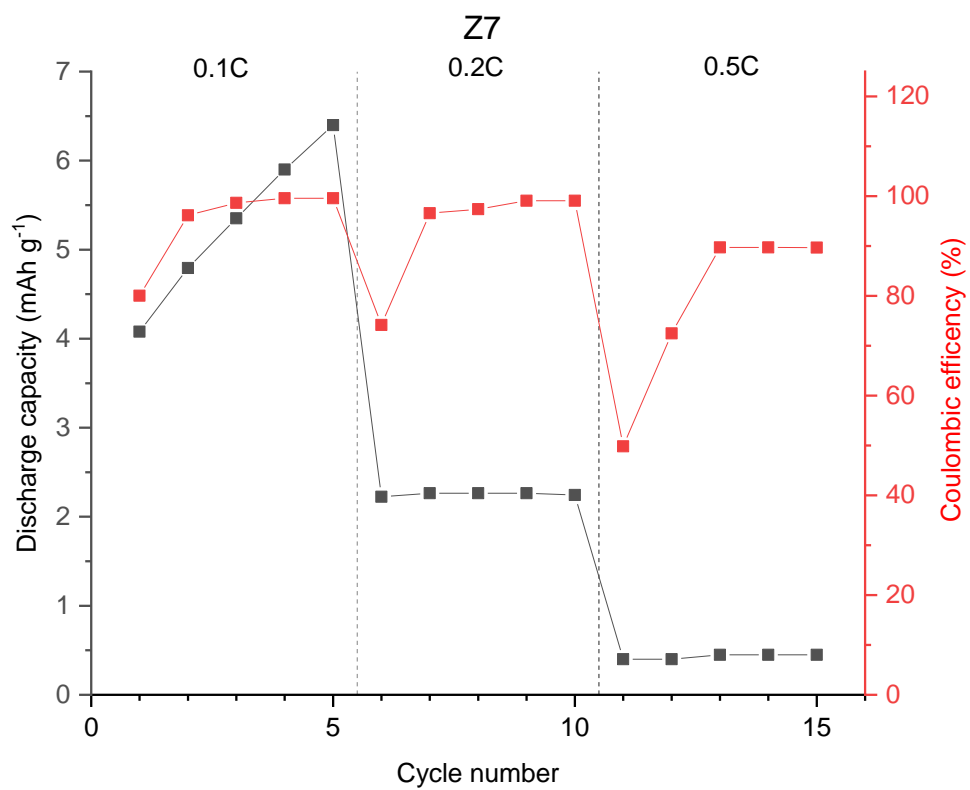

Supplementary figure 31. (a) CI battery. Loss of contact with T-treatment with 2 collectors of internal pressure, and. (b) C2 battery. Short-circuit due to heavy P-treatment of 140 g cm^{-2}.
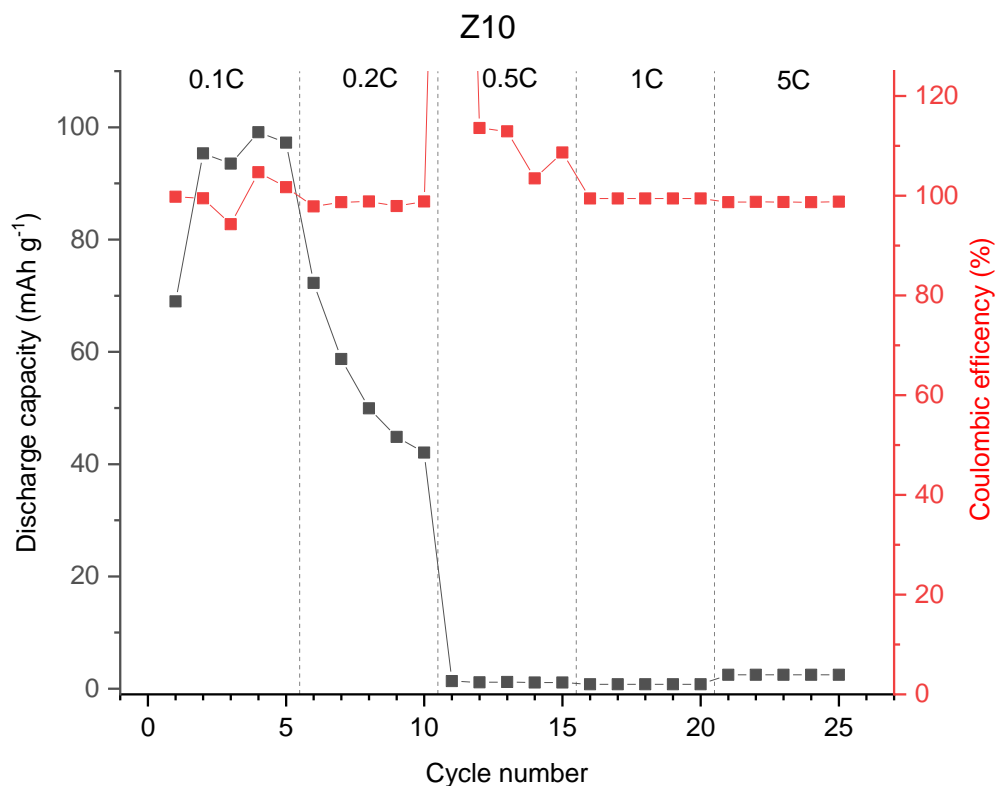
Supplementary figure 32. Cycling of battery C3.

Supplementary figure 33. Cycling of battery C4.

Supplementary figure 34. Cycling of battery Z7.

Supplementary figure 35. Cycling of battery Z10.